Design of the high Pressure HIgh temperature annuLUS flow (PHILUS) Facility

Ali Haydar Karabacak

Thesis submitted to the Faculty of the

Virginia Polytechnic Institute and State University

in partial fulfillment of the requirements for the degree of

Master of Science

in

Nuclear Engineering

Juliana P. Duarte, Chair

Mark Pierson

Yang Liu

May 6, 2022

Blacksburg, Virginia

Keywords: High Pressure Loop, Critical Heat Flux (CHF), post-CHF, Design

Design of the high Pressure HIgh temperature annuLUS flow (PHILUS) Facility

Ali Haydar Karabacak

(ABSTRACT)

Critical heat flux (CHF) and post-CHF are two critical phenomena in light water-cooled nuclear power plants regarding safety. Even though the general trends of CHF and post-CHF are known, the exact mechanisms are still unknown. To better understand CHF and post-CHF, experimental flow boiling facilities are constructed around the world. However, these facilities are limited in their experimental conditions and spatial resolution necessary to advance our understanding of two-phase heat transfer. Previous rod surface measurements were collected with thermocouples to measure CHF location and temperature excursion, yet thermocouples provide limited spatial resolution, which leads to significant uncertainties in the CHF prediction. On the other hand, optical fiber temperature sensors can measure the temperature and the CHF propagation with high spatial resolution. Also, the capability of the optical fiber at high temperatures has been proven in previous studies. The current study aims to apply optical fiber at high-pressure and high mass fluxes. The high-Pressure HIgh-temperature annuLUS flow (PHILUS) facility was designed to provide desired working conditions in the test section that uses optical fiber temperature sensors. The PHILUS test section has a length of 1320 mm, with 1000 mm of heated length. The working conditions of the PHILUS are up to 18 MPa, temperatures up to 357°C, and coolant mass flux from 500 to 3700 kg/m^2s. The main components of the loop are a steam separator, two heat exchangers (a condenser and a cooler), a bladder-type accumulator, two bypass lines, and

a high-pressure pump. Coolant-Boiling in Rod Arrays-Two Fluids (COBRA-TF) code was used to design the CHF and post-CHF experiments to be performed at the PHILUS facility.

Design of the high Pressure HIgh temperature annuLUS flow (PHILUS) Facility

Ali Haydar Karabacak

(GENERAL AUDIENCE ABSTRACT)

A nuclear power plant produces heat which is transferred from the reactor core through the coolant. The coolant water flows through the reactor core to safely transport the heat that ultimately is used to produce electrical energy. If the balance between the power produced by fission and the energy removed by the coolant is changed, it can lead to potential damage to the reactor core. The maximum heat transfer rate occurs at the point where a vapor blanket covers the surface of the fuel cladding. At this point, known as Critical Heat Flux (CHF), the surface temperature drastically increases. To better understand and better predict the CHF, experimental facilities are needed. Even though there are several facilities worldwide, most of them have limited working conditions and measurement capabilities. Past experiments used thermocouples to measure the surface temperature with a very small spatial resolution, which causes very large uncertainties in the CHF and post-CHF predictions. On the other hand, optical fiber sensors can be used to measure temperature with very high spatial resolution. The high-Pressure HIgh-temperature annuLUS flow (PHILUS) facility was designed in this work to apply optical fibers in the measurement of the rod surface temperature and simulations were performed to show its advantages. The working conditions of the PHILUS are comparable to commercial pressurized water reactors.

Dedication

I want to dedicate this work to my lovely wife and family, who supported me every moment in my life.

Acknowledgments

I want to thank Dr. Juliana Duarte for her guidance and support throughout my research. I also want to thank my committee members, Dr. Yang Liu and Dr. Mark Pierson. I would like to thank my friends at the HEATS lab, especially Paul Hurley, Dr. Kyung Mo Kim, Jeric, Matt, Daniyal, Max, and Mohsen, for giving me advice and helping me finish my research. Also, I want to thank Yunus Eren Akın, Kenan Burak Aydın, Emre Karagülle, Mahmud Esad Uluer, and Uğur Bozdoğan who always helped me in Blacksburg. I also want to thank the Turkish Government for its financial support throughout my master's education. And most importantly, I want to thank to my whole family. Without them, nothing matters.

Contents

List of Figures x

List of Tables xiii

1 Introduction 1

1.1 Critical Heat Flux (CHF) 2

2 Review of Literature 4

2.1 Two-Phase Heat Transfer Regimes 4

2.1.1 The Pool Boiling Curve 4

2.1.2 Nucleate Boiling Region ($B - C$) 6

2.1.3 Critical Heat Flux 6

2.1.4 Transition Boiling Region ($C - D$) 7

2.1.5 Film Boiling Region ($D - F$) 7

2.2 Description of loops around the world 8

2.2.1 The Post-CHF Heat Transfer (PCHT) test facility 8

2.2.2 The reactor coolant system thermal-hydraulic loop (RCS loop) facility 10

2.2.3 The high-pressure water test (HWAT) loop 12

2.2.4 The platform experimental thermal-hydraulics (Pether) facility . . . 15

2.2.5 The Flow boiling thermal-hydraulic circuit 17

3 Design of the PHILUS **22**

3.1 Test section 23

3.1.1 Optical Fibers 28

3.2 Piping 29

3.2.1 Primary piping 29

3.3 Steam Separator 33

3.4 Heat Exchange components 34

3.4.1 Condenser 35

3.4.2 Cooler 37

3.4.3 Calculation of Required Heat Transfer Surface 38

3.5 High Pressure pump 44

3.6 Accumulator 49

3.7 Valves 53

3.8 Data acquisition system 54

3.8.1 DAQ system hardware 55

3.9 Instrumentation 57

3.10 Secondary Loop 59

3.11 Support structure 61

4 COBRA-TF (CTF) Simulation **65**

4.1 COBRA-TF 65

4.2 COBRA-TF on the PHILUS 67

4.2.1 Comparison of the DNB check options 69

4.2.2 CHF Power 71

4.2.3 Necessary Heat Flux at CHF 73

4.2.4 Direct Comparison with Groeneveld Look Up Table 75

4.2.5 Void Fraction 77

4.2.6 Pressure Drop in the Test Section 81

4.3 Simulation of Barnett's data 83

5 Conclusions and Future Work **85**

Appendices **92**

Appendix A Components and Working Conditions of Investigated Facilities **93**

Appendix B Sample Input File for CTF **94**

Appendix C Results of CTF simulations **104**

List of Figures

1.1 World Total Final Consumption by Source 1971-2019 [2] 1

2.1 Pool Boiling Curve for Saturated Water at Atmospheric Pressure [13] 5

2.2 Schematic diagram of the PCHT Facility [3] 10

2.3 Schematic diagram of the KAERI RCS Facility [4] 12

2.4 Schematic diagram of the HWAT Facility [18] 15

2.5 Schematic diagram of the Pether Flow Loop [20] 17

2.6 Schematic diagram of the Flow Boiling Hydraulic Circuit [21] 19

2.7 Summary of Design Specifications of Investigated Flow Boiling Facilities . . 20

3.1 The CAD drawing of the PHILUS facility 22

3.2 (Left) Test Section Schematic and (Right) Photo of the Test Section 24

3.3 PWR Subchannel cross-section [13] 24

3.4 Top view of the heater rod 26

3.5 Schematic of the Optical Fibers 28

3.6 Dimensions of 3/4 inches the Sch-160 SS 316/L 30

3.7 Side view of socket weld 90° elbows to ASME B16.11 class 6000 31

3.8 Side view of 2500 # raised face socket weld sch 160 bore flange 32

3.9 (Left) Schematic of the Steam Separator and (Right) Picture of the Steam Separator . . . 34

3.10 (Top) Schematic of the Condenser and (Bottom) Picture of the Condenser . 35

3.11 (Left) Schematic of the Cooler and (Right) Picture of the Cooler 37

3.12 Correction factor for different flow types 40

3.13 (Left) Schematic of the High-Pressure Pump and (Right) Picture of the High-Pressure Pump 44

3.14 Cross-sectional view of the accumulators 50

3.15 Schematic diagram of the PHILUS Facility 58

3.16 Moody diagram for the friction factor [29] 60

3.17 Front and side views of the support structure 61

3.18 Bolting the support structure 62

3.19 (Left) The Schematic of the Test Section Connection (Right) Picture of the Test Section Connection 63

3.20 The PHILUS Facility 64

4.1 CTF subchannels 66

4.2 Iterative Procedure to Determine the Predicted CHF Value and Associated Properties 68

4.3 Axial schematic of the PHILUS Facility Test Section 69

4.4 Test section power at CHF at 500-3000 $^{kg}/_{m^2 s}$ 72

4.5 Test section power at CHF at 3500 $^{kg}/_{m^2s}$ 73

4.6 CHF at 500-3000 $^{kg}/_{m^2s}$ 74

4.7 CHF at 3500 $^{kg}/_{m^2s}$ 75

4.8 Comparison of CTF Local Heat Flux and Look-Up Table Hand calculation . 76

4.9 Flow Regime Selection Logic [31] 78

4.10 Flow Regime Recognized by CTF [31] 78

4.11 Void Fraction and Flow Regime at 500-3000 $^{kg}/_{m^2s}$ 80

4.12 Void Fraction and Flow Regime at 3500 $^{kg}/_{m^2s}$ 81

4.13 Pressure Drop at 500-3000 $^{kg}/_{m^2s}$ 82

4.14 Pressure Drop at 3500 $^{kg}/_{m^2s}$ 83

4.15 Comparison of Barnett's data and its CTF simulation 84

List of Tables

2.1 Geometrical Information of the PCHT test section [3] 9

2.2 Geometrical Information of the RCS facility test sections 11

2.3 Geometrical Information of the HWAT test sections 13

2.4 Geometrical information of the Pether flow loop's test sections [6] 16

2.5 Geometrical Information of the McMaster University's test section [7] 18

3.1 Physical Properties of Zirconium 702 and Inconel 600 26

3.2 Specification of the Test Section 27

3.3 Specification of the Thermocouple 27

3.4 ANSI/ ASME B36.10M Standards for thickness 30

3.5 Working Pressure Between 400-800 Fahrenheit Degrees 31

3.6 Dimensions of socket weld 90 elbows to ASME B16.11 class 6000 31

3.7 Comparison of the Flanges, Hubs, and Clamps 32

3.8 Dimensions of 2500 # raised face socket weld Sch 160 bore flanges 33

3.9 Design and Working Parameters of the Steam Separator 33

3.10 Test conditions and TRACE predictions for determining heat removal requirements (courtesy from Paul Hurley) 36

3.11 Hand Calculated Specification of the Cooler 42

3.12 Required Heat Transfer Surface 43

3.13 Specification of the Heat Exchange Components 43

3.14 Specification of the Pump 45

3.15 Total pressure head simulation in unheated test section in TRACE simulation 48

3.16 Specification of the Accumulator 52

3.17 Specification of the Lift Check Valve 53

3.18 Specification of the filling valve 54

3.19 cRIO module specification 55

3.20 Modules and purpose 56

3.21 Modules and specifications 56

3.22 Specification of the instrumentation 59

3.23 Specification of low-pressure pump 60

3.24 Specification of tubes in the support structure 62

4.1 CTF main model choices 67

4.2 Range of Operating Conditions of DNB check option 70

4.3 Local Heat Flux of W-3, Biasi, and Groeneveld at CHF 71

5.1 Undefined Components Situations 87

A.1 Main components of the investigated loops 93

C.1 CTF results for 7 MPa 104

C.2 CTF results for 9 MPa 105

C.3 CTF results for 11 MPa 106

C.4 CTF results for 13 MPa 107

C.5 CTF results for 15 MPa 108

C.6 CTF results for 17 MPa 109

List of Abbreviations

α Void Fraction)

β Volumetric Flow Fraction (-)

ΔP Pressure Drop (kPa)

ΔT_{LM} Logarithmic mean temperature differences

$\dot{m}$ Mass Flow (kg/s)

$\dot{Q}_{Cond.}$ Power of the Condenser (kW)

$\dot{Q}_{Cooler}$ Power of the Cooler (kW)

ρ Density(kg/m^3)

h_f, h_g Specific Enthalpy(kJ/kg)

h_s Heat transfer coefficient of the shell side ($W/(m^2K)$)

h_t Heat transfer coefficient of the tube side ($W/(m^2K)$)

h_{fg} Specific Heat of vaporization (kJ/kg)

q'' Heat Flux(kg/m^2s)

x quality (-)

ASME American Society of Mechanical Engineers

BWRs Boiling Water Reactors

CFD Computational Fluid Dynamics

CHF Critical Heat Flux

Cobra-TF Coolant-Boiling in Rod Arrays-Two Fluids

CTF Updated version of COBRA-TF

DAQ's Data Acquisition Systems

DBAs Design Basis Accidents

g Acceleration of gravity (m/s^2)

H Overal heat transfer coefficient ($W/(m^2K)$)

HWAT The high-pressure water test

IAFB Inverted annular film boiling

IASB Inverted slug film boiling

k thermal conductivity (W/mK)

KAERI Korean Atomic Energy Research Institute

LOCAs Loss-of-coolant accidents

LWRs Light Water Reactors

MDNBR The minimum departure from nucleate boiling ratio

NPSH The required net positive suction head

PCHT The Post-CHF Heat Transfer test facility

Pether platform for the experimental thermal-hydraulics

PHILUS The high-Pressure HIgh-temperature annuLUS flow facility

Pr Prandtl number

PWRs Pressure Water Reactors

RCS loop The reactor coolant system thermal-hydraulic loop

Re Reynolds number

T/H Thermal-Hydraulic

TRACE The TRAC/RELAP Advanced Computational Engine

VFD Variable frequency drive

Chapter 1

Introduction

In the past decades, the energy consumption of the world has been increasing, as shown in Figure 1.1. This increase will accelerate with the population growth and new-technology, such as electric cars and electronic devices applied in the health system, transportation, and smart cities. Nuclear energy is one of the cleanest and safest ways to meet this increasing demand. However, nuclear reactors encompass several complex phenomena, and the critical heat flux (CHF) is one of the most important. CHF was described in 1934 by Shiro Nukiyama [1] as the maximum point in the two-phase heat transfer curve, and it has been studied for almost 90 years. Several research studies contributed to understanding CHF general trends, but the exact CHF mechanisms are still unknown. The CHF phenomenon is very complex, and the existing prediction methods are insufficient alone to describe it. Therefore, additional experimental data is still required.

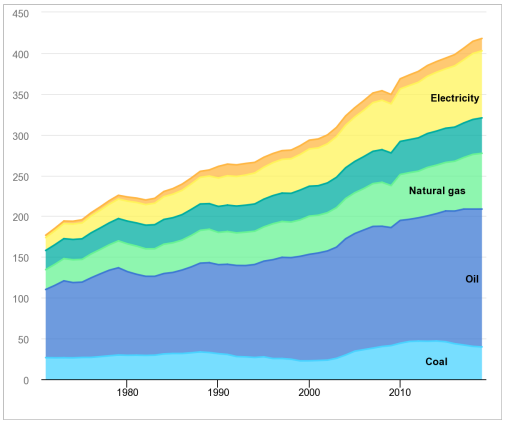

Figure 1.1: World Total Final Consumption by Source 1971-2019 [2]

Flow boiling facilities have been constructed over the years around the world to investigate CHF [3–7]. Some of the experimental facilities are discussed in this thesis. The comparison among these facilities reveals that most of them have very limited working conditions or a very low spatial resolution in the surface temperature measurement. The low spatial resolution causes large uncertainties in CHF prediction and the understanding of post-CHF heat transfer. With the advancements in the optical fiber temperature sensors, these sensors can be used in two-phase flow channels with very high spatial resolution and high fidelity.

1.1 Critical Heat Flux (CHF)

Critical heat flux (CHF) is one of the most vital safety phenomena for several two-phase heat transfer applications, such as light water-cooled nuclear power plants [8]. CHF is a phenomenon that occurs in a two-phase flow characterized by the formation of a vapor layer on a heated surface, which causes a severe reduction in the heat transfer coefficient [9]. If CHF happens, the coolant's capability to remove heat from the cladding surface considerably decreases, leading to a rapid rise in the cladding temperature and possible fuel failure. Therefore, understanding the nature of the CHF and the post-CHF at any flow condition is essential for Light Water Reactors (LWRs). CHF is one of the design limits for nuclear power plants. For example, for LWRs, the cladding temperature should not exceed the reactor design limit (*e.g.* 1204 $^{\circ}C$ for Zircolay cladding). Another example for Pressurized Water Reactors (PWRs), the CHF should not achieve the minimum departure from nucleate boiling ratio (MDNBR) during certain Design Basis Accidents (DBAs). Accurate prediction of CHF is then essential to avoid the departure from nucleate boiling (DNB), which is CHF-type at low qualities [10]. At high qualities, the CHF phenomenon is known as dryout. Boiling Water Reactors (BWRs) are where a film of liquid coolant surrounding the rod

surface dries out at the CHF point.[11].

Hence, this thesis describes the design of the high-Pressure HIgh-temperature annuLUS flow (PHILUS) Facility at Virginia Tech. The PHILUS is designed to use optical fiber as a temperature sensor under Pressurized Water Reactor (PWR) conditions. The main components of the PHILUS are the test section, a steam separator, a condenser, a bladder accumulator, a cooler, two bypass lines, and a high-pressure pump. The TRAC/RELAP Advanced Computational Engine (TRACE) was used to simulate the facility during the design phase. TRACE is a thermal-hydraulic code, and it was used to calculate the required specification of various components. TRACE has been designed to perform best-estimate analyses of loss-of-coolant accidents (LOCAs), operational transients, and other accident scenarios in PWRs and BWRs [12]. TRACE was specifically used to calculate the quality at CHF conditions, and the total pressure drop of the loop. TRACE was also used to estimate the bypass valves requirements,*i.e.* the mass flux while each valve was open, partially open, or closed. TRACE simulations were essential during the design for several reasons. Two-phase pressure drop simulations in the entire loop are one of the most important outputs of TRACE simulation. Additionally, CTF, the updated version of Coolant-Boiling in Rod Arrays-Two Fluids (Cobra-TF), has also been used during the design of the PHILUS facility. CTF is a 1-D transient code that solves energy, mass, and axial and transverse momentum equations for fluid film, vapor, and liquid droplets. In CTF, only the test section is simulated under the working conditions of the PHILUS facility. CTF simulation results will be used to guide future experiments.

Chapter 2

Review of Literature

2.1 Two-Phase Heat Transfer Regimes

Boiling heat transfer occurs at operational conditions in both PWR and BWR cores. A better understanding of boiling heat transfer is essential to increase efficiency and safety in the reactor cores since a sufficient margin between the CHF and the maximum local heat flux is one of the essential parameters in the reactor plant's design, as previously discussed. Five specific CHF facilities related to LWR reactors are described in this chapter. They are located at research universities and research institutes.

2.1.1 The Pool Boiling Curve

In 1934, Nukiyama discovered the maximum and minimum heat fluxes as boundaries of the two-phase heat transfer regimes [1]. Imagine a solid surface that is heated by a source and surrounded by a liquid pool. After the solid surface temperature passes the saturation temperature by a certain amount (*i.e.*, reach the onset of nucleate boiling or ONB), the heated surface starts to generate vapor through the boiling process. The logarithmic plot of the surface heat flux and the temperature differences between the wall and saturation ($T_w - T_{sat}$) has been illustrated in the boiling curve, as shown in Figure 2.1 [13]. The reason for the peak is due to vapor instability in rising bubble columns on the surface. The bubbles

coalesce at the high heat fluxes as they rise and form isolated columns.

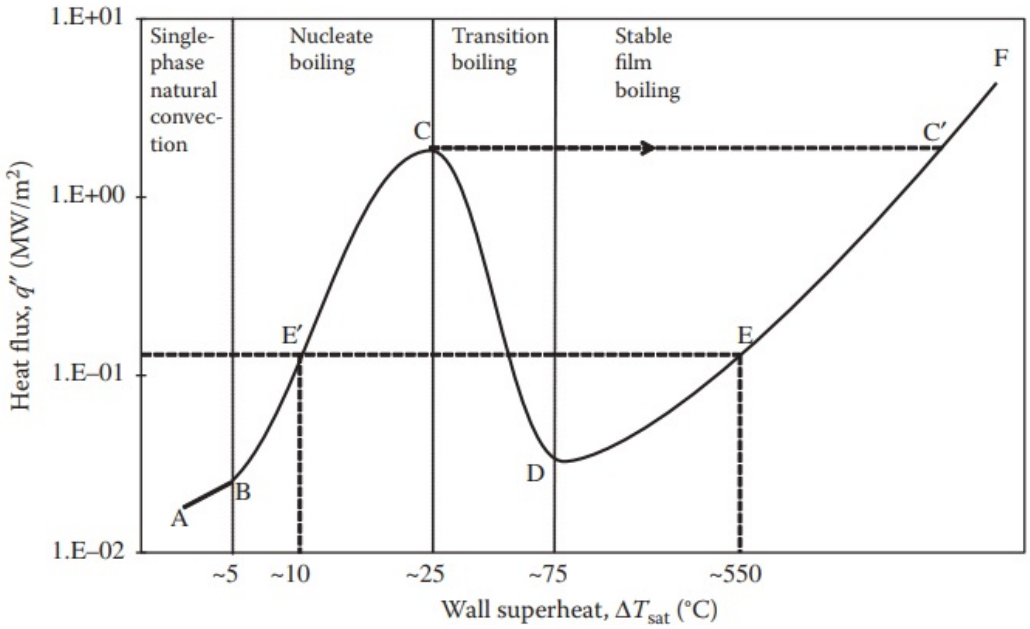

Figure 2.1: Pool Boiling Curve for Saturated Water at Atmospheric Pressure [13]

As it can also be seen in Fig. 2.1 after the B point, the heat transfer is more effective due to the bubble formation, so the heat flux in this region $(B-C)$ is much higher than the heat flux in the single-phase natural convection region. The transient region $(C-D)$ is characterized by the unstable vapor film at the surface, while the vapor film is stable at higher heat fluxes $(D-F)$. Point C is the critical heat flux condition, and point D is called the Leidenfrost (or the minimum stable film boiling temperature). The transition boiling region can only be seen if the wall temperature is controlled. However, in most boiling engineering applications, q'' is the variable input, and ΔT cannot be controlled, so with a constant heat flux at point C, the surface temperature suddenly increase to the point C'.

2.1.2 Nucleate Boiling Region ($B - C$)

The nucleate boiling region ($B - C$) starts at the onset of nucleate boiling (point B), where boiling can be first observed. If the liquid temperature is below saturated temperature, subcooled nucleate boiling exists, and the bubbles collapse after detaching from the wall. If the temperature reaches the saturation temperature with the heat flux increase, bubbles will detach from the surface and exist in the liquid bulk. With the increase of the heat flux, the number of nucleate size increases, and the size of the bubbles increase and start to combine into larger bubbles. It is known that boiling usually occurs at the nucleation sites, which depends on the wettability of the fluid-solid pair, surface profile, and the wall super-heat [13]. Because of these complexities, there is no complete theoretical correlation in this region[13].

2.1.3 Critical Heat Flux

The CHF occurs at point C in Figure 2.1. For a constant heat flux at point C, the surface temperature suddenly increases to C'. At this point, vapor covers the surface, and the heat transfer from the coolant to the wall is drastically impaired due to the vapor blanket formed.

CHF depends upon several variables, including local quality, pressure, mass flux, flow geometry, and power profile. CHF increases with an increase in inlet sub-cooling, and mass flux [9]. However, CHF increases with pressure to one point (around 5-6 MPa for water) and then starts to decrease with higher pressure. Existing Computational Fluid Dynamics (CFD) codes cannot predict CHF accurately due to the complex two-phase flow conditions. Hence experimental correlations are commonly used for better estimation of the CHF values. Because of the dependency of CHF data on the above variable ranges, correlations have limited applications. Unique correlations might be needed for a round tube, square channel,

annulus, rod bundles, or other geometries.

Because of the needed data for the CHF, there are facilities around the world to collect data for various flow conditions. Some of these facilities are explained in Section 2.2.

2.1.4 Transition Boiling Region ($C - D$)

A unique feature of the transition boiling region ($C - D$) is that this region can only be obtained during a steady-state condition if the surface temperature is controlled. This unique feature is the reason that Nukiyama did not observe this region in his experiment since he controlled heat flux (q'') and measured $\Delta T = T_{wall} - T_{sat}$. With the heat flux increase, the wall temperature will follow the path $C - C' - F$. With the decrease of the heat flux, the path is $F - C' - E - D - B$. This regime is notoriously difficult to model analytically or numerically. It is characterized by unstable or partial film boiling. At any point, the conditions can oscillate between film and nucleate boiling.

2.1.5 Film Boiling Region ($D - F$)

In the film boiling region, the vapor covers the surface of the cladding. Heat is transferred across the vapor to the two-phase mixture. For the minimum film boiling temperature (D), there are several correlations to predict the temperature as a function of pressure and subcooling, for example, [13]. Berenson[14] derived a formulation that the temperature only depends on the fluid properties while Henry [15] recommended two correction factors for Berenson's formulation: i) an interface contact effect and ii) a liquid sub-layer evaporation effect. On the other hand, Groeneveld and Stewart developed a correlation that depends only on pressure and subcooling [16] The uncertainties associated with the minimum film boiling temperature are one of the motivations for designing and building the PHILUS facility.

2.2 Description of loops around the world

Experimental data are essential to improve CHF correlations, and it is the reason there are loops to investigate CHF under various conditions around the world. Some of the loops, their functionality, main components, controlled parameters, and measurements are explained in this section. During this explanation, test sections are specifically investigated to show the unique features of the PHILUS (high Pressure HIgh temperature annuLUS flow) facility.

2.2.1 The Post-CHF Heat Transfer (PCHT) test facility

The Post-CHF Heat Transfer (PCHT) test facility was initially designed at The Ohio State University and then moved to the University of Michigan. The PCHT test facility aims to improve the database of modeling inverted annular film boiling (IAFB) and inverted slug film boiling (ISFB) to enhance reactor safety [3]. The facility was designed to acquire data to improve current prediction models. The test section of the PCHT facility is a directly heated circular tube with 34 kW power. The parameter's range was designed to cover the quasi-state IAFB and ISFB regime test. The pressure range of the PCHT facility is from 0.14 MPa to 3.45 MPa, with the mass flux between 150 and 200 $kg/m^2 \cdot s$, and inlet subcooling is up to $50°C$. With the safety margin, all components have ASME code to work under 6.89 MPa at $300°C$. Some geometric information of the test section can be seen in Table 2.1. However, the working conditions of the PCHT are much lower than the operating conditions of a nuclear reactor, so it will only acquire data under accident conditions. Limited pressure, flow rate, and low spatial temperature resolution are other drawbacks of the PCHT.

The facility uses a reservoir tank for degassing, water storage, and rough temperature control. It can store 115 L of water to adjust the system temperature with the help of thermal inertia. Also, electric heaters (45 kW) are used for water degassing and controlling the inlet

Table 2.1: Geometrical Information of the PCHT test section [3]

Items	**mm**
Total length	1510
Heated section	1000
Total unheated length from top and bottom	460
Total hot patch section from top and bottom	50
Diameter of the tube	19.05 (3/4")

temperature of the test section.

A condenser, a pre-cooler, and a pre-heater are used to control the water temperature in the facility. The condenser (35 kW) is located between the outlet of the test section and the pressurizer to condense the steam-water mixture. The pre-heater (5 kW) and the pre-cooler (5 kW) are used to achieve the desired inlet temperature at the test section. The pre-heater and the pre-cooler water temperature can heat or cool $4°C$ at the highest mass flux. One of the purposes of the pre-cooler is to ensure the water temperature at the inlet of the pump is lower than the saturation temperature. Pressure is controlled with a pressurizer that has 0.076 m^3 capacity with three electric heaters (total power 13.5 kW). The pressurizer is also used for degassing the water, along with the reservoir tank, during the experimental run. The pressurizer's water level is monitored with a differential pressure transducer.

There are two flow meters between the regulating valve and pre-heater to measure the flow rate of the loop. Void fraction and the characteristics of the flow structure are measured with a gamma course system that was developed by the University of Michigan [3]. A schematic diagram of the PCHT facility can be seen in Figure 2.2.

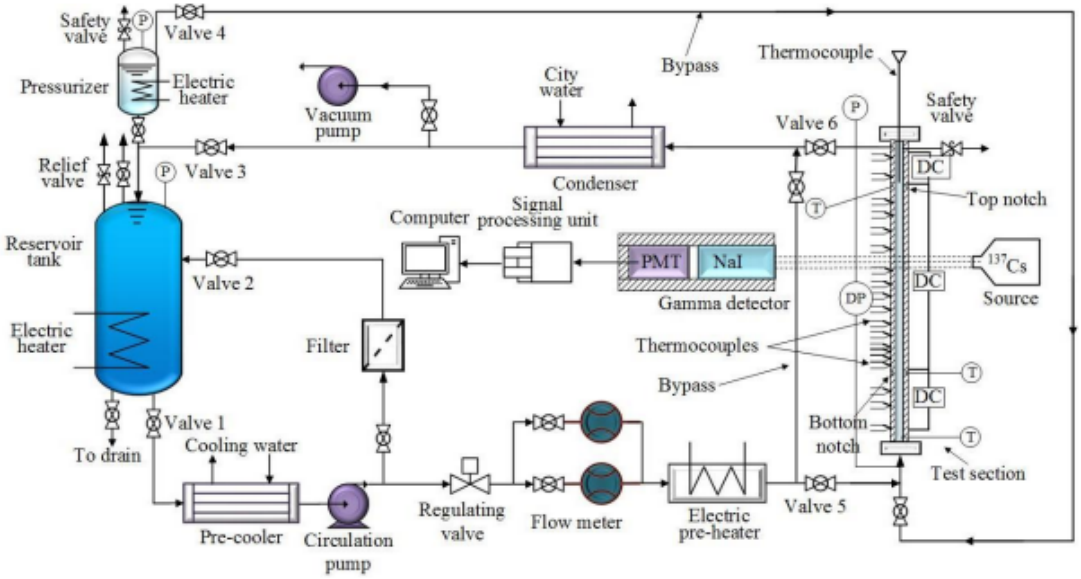

Figure 2.2: Schematic diagram of the PCHT Facility [3]

2.2.2 The reactor coolant system thermal-hydraulic loop (RCS loop) facility

The main objective of the reactor coolant system thermal-hydraulic loop (RCS loop) facility at KAERI (Korean Atomic Energy Research Institute) is wide working conditions for having a deep knowledge of the effects of various parameters on post-CHF [4]. During the first design, the test section was an internally heated annulus flow channel [17]. After that, it was replaced with a 3x3 rod bundle. The total power of the 9 rods is 470 kW, and each rod has a 3673 mm heated length. Also, the test section has a symmetric cosine heat flux profile. Table 2.2 shows the geometrical information of the test sections of the RCS facility. For both test sections, the working conditions are between 0.5 and 16.0 MPa with up to 3180 kg/m^2·s, and inlet subcooling is between 85-413 kg/kJ [17]. The working conditions are comparable to a Pressurized Water Reactor; however, the instrumentation is limited to

observing the specific location and local temperatures of the CHF because of the limited number of thermocouples.

Table 2.2: Geometrical Information of the RCS facility test sections

Items	**1st Test Section**	**2nd Test Section**
Heated length each rod (mm)	1842	3673
Total length of flow housing (mm^2)	-	39.8×39.8
Outer diameter (mm)	19.4	-
Pitch (mm)	-	12.6
Inner heater rod's outer diameter (mm)	9.54	9.52
Thermocouple location from top of the heated section (mm)	10, 30, 110, 310, 510, 910	10, 225, 625, 1425, 1825

The RCS loop uses de-ionized water for tests, and a circulation pump and a flow control valve are used to control the inlet flow rate of the water. Flow fluctuations that usually occur during a low flow condition are prevented with a throttling valve located at the inlet of the test section. A preheater (40 kW) is used to control the inlet temperature of the test section. After steam and water are separated in the separator, steam condenses in a condenser attached to the separator, which is necessary for the closed loops to prevent mass loss. A pressurizer with a 40 kW powered heater is used to pressurize the loop. A schematic diagram of the RCS loop can be seen in Figure 2.3. In the test section of the RCS loop, there are eleven spacer grids to support the heater rods in the test section. Also, thermocouples are installed just upstream of the spacer grids. Six or four K-type thermocouples are embedded on the heater surface to measure the temperature of the heater rod's surface and detect CHF occurrence. Sixteen same-type thermocouples are installed at the inlet and the outlet of the

heated section to measure the subchannel fluid temperature.

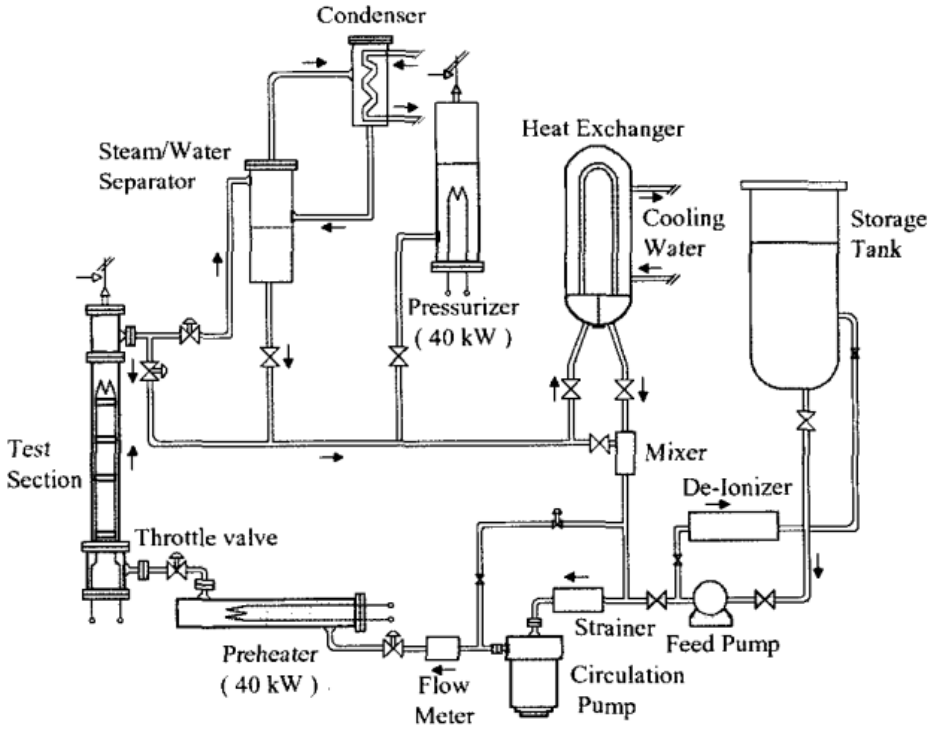

Figure 2.3: Schematic diagram of the KAERI RCS Facility [4]

2.2.3 The high-pressure water test (HWAT) loop

The high-pressure water test (HWAT) loop of the Royal Institute of Technology (KTH, Stockholm, Sweden) is designed to investigate post-dry-out heat transfer in annuli with flow obstacles [5]. The test section (annulus) consists of two concentric heated pipes with three types of obstacles: pin-spacers, cylindrical, and grid obstacles. During the experiments, pin-spacer obstacles are used for reference. The other two additional obstacles are attached inside the channel when the pin spacer is still in it to measure the effect of the obstacles on the heat transfer. The HWAT loop is designed to operate up to 25 MPa with working fluid

temperature up to 340 $^{\circ}C$ [18]. However, the test section has a lower pressure limit of 18.3 MPa. The testing conditions of the one set of the experiments [18] were 5 to 7 MPa with from 500 to 1750 kg/m^{2}s mass flux at 10 to 40 K inlet subcooling. Another set of experiments were performed at 7 MPa with the mass flux range of 500-1500 kg/m^{2}s, and the inlet subcooling 10-40 K [19]. Also, low spatial resolution across the heater rod's axial direction limits the HWAT loop for temperature measurement. Table 2.3 shows the geometrical information of the HWAT's test sections.

Table 2.3: Geometrical Information of the HWAT test sections

	Obstacle type		
Items	**Pin Spacer**	**Pin Spacer and Cylindrical**	**Pin Spacer and Grid**
Blockage area of the obstacle (%)	10.13	7.3	10.07
Total length (mm)	3650	3650	3650
Obstacle length (mm)	-	20	40
Obstacle position from bottom to top (mm)	520, 1000, 1750, 2580, 3258	2996, 3372	2996, 3418

The water is filtered to have less than 0.005 micro-siemens electrical conductivity. A feed-water pump is used to deliver water to the loop. Besides feeding the loop, the feed pump's purpose is to increase the pressure to the desired value. The feed pump is one of the unique parts of the HWAT loop because the feed pump is the only component to increase the pressure in the loop. With the help of the circulation pump, the flow is maintained in the main loop. It is essential to control the temperature at the inlet of the circulation pump during the experiment to prevent cavitation. This is why the upper limit of the coolant temperature is 30 K lower than the saturation temperature. There are two serial connected preheaters, and one of them (155 kW) controls the inlet temperature of the test section. However, there

is a heat loss between the inlet of the test section and the outlet of the preheater. The second preheater is connected before the inlet of the test section to solve this problem and refine the inlet temperature. Also, there is a blow-off valve to control the pressure and, more importantly, release the fluid from the loop during an emergency case. There are 88 thermocouples to record the wall temperature of the test section, and 40 of them are located inside the inner rod axially, while the remaining are outside the outer pipe. With the help of a Barton cell device and a Statham differential pressure transducer, pressure drop in the test section is measured. The Barton cell (differential pressure recorder) is necessary to calculate the static pressure, which is the input parameter to calculate the saturation temperature. There are two different types of flow measurement systems. One type of flow measurement is a turbine flow meter that measures the volume flow rate with the help of a 6-bladed rotor. The other system is made of a four-pipe system where the Barton cells are located [18]. A schematic diagram of the HWAT facility can be seen Figure 2.4

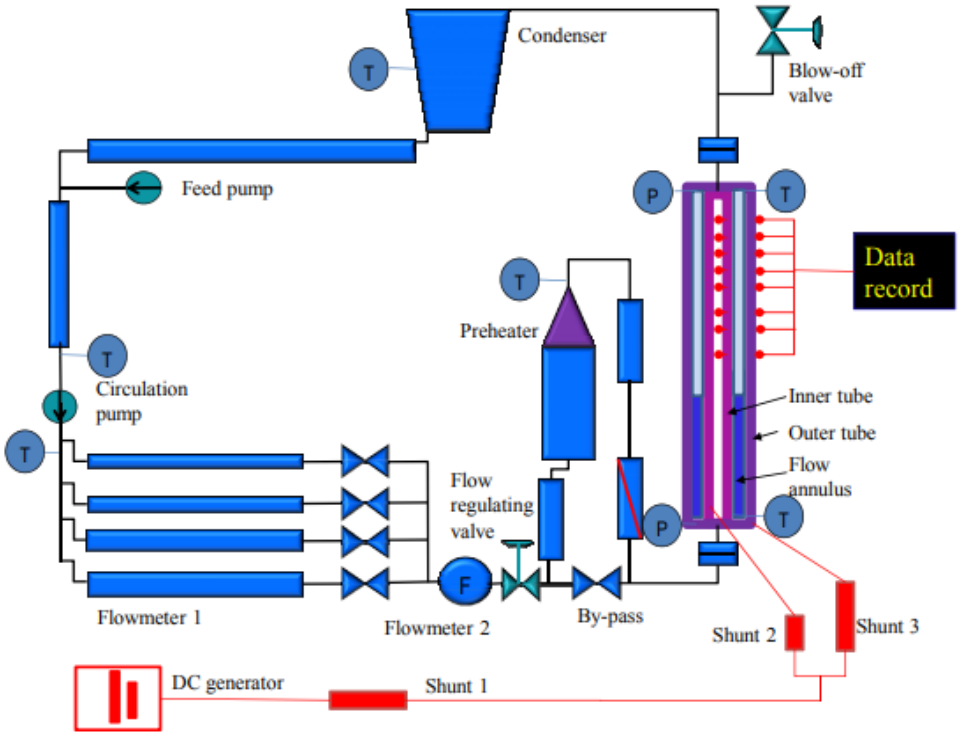

Figure 2.4: Schematic diagram of the HWAT Facility [18]

2.2.4 The platform experimental thermal-hydraulics (Pether) facility

The objective of the platform for the experimental thermal-hydraulics (Pether) facility, constructed at the Massachusetts Institute of Technology (MIT), is to investigate the subcooled flow boiling quantities (nucleation site density, bubble growth, etc.) up to CHF with a high-speed video camera and high-speed InfraRed (IR) camera [6]. In the test section, there are three openings to accommodate quartz windows, and the remaining opening is for the installation of the heater cartridge with a 5 kW uniform power. The test section measures 22 cm tall and 12.7 cm in diameter at its widest. For the test section, the pressure range is from ambient to 1 MPa, and the working temperature and the mass flux are up to saturation

temperature ($179.88°C$) and 0 to 2000 kg/m^{2}s, respectively. Geometrical information of the section can be seen in Table 2.4. Even with visualization windows and two-phase flow high spatial temperature measurement resolution using IR thermometry, the maximum pressure limit cannot allow them to collect data for the high pressure.

Table 2.4: Geometrical information of the Pether flow loop's test sections [6]

Item	**mm**
Length of the test section	220
Diameter of the test section	127
Windows and heater length	100

A circulation pump (a variable speed pump) allows different flow rates by changing the output pump head. A hydropad accumulator has been used to overcome pressure oscillation. The accumulator is connected to the highest location of the loop to pressurize the facility. Filters and degassing systems are used to maintain quality water.

There are three different degassing systems; one of them is a PermSelect degassing system that is used to remove non-condensable gases. This system uses a gas-permeable silicon membrane system that separates the liquid from a vacuum. With the help of the pressure differential between liquid and a vacuum that is created with a vacuum pump, the gasses pass through the membrane. However, this system can only work under atmospheric pressure and temperature. Therefore, the high-temperature degassing line has been connected to the top of the test section. This system uses the heater in the loop to boil the water and ventilate the vapor from the venting point. This process should be done till the non-condensable gases are purged. This method is a high-pressure and high-temperature degassing system. The last degassing system of the facility is a vacuum pump used for initial vacuum and degassing.

A heat exchanger is used to remove heat from the water in the main loop. The heat exchanger

also ensures that the water's temperature is lower than the saturation temperature, which prevents cavitation problems in the circulation pump. For high mass flux conditions, the pressure drop is significant. Because of the pressure drop, the pump's inlet pressure might be lower than the net positive suction head pressure (NPSH), which leads to cavitation in the pump. However, the solution to this problem is to cool water before the inlet of the test section, which helps to lower the required NPSH and prevent cavitation. Also, a preheater, which is a pipe heater, is used to maintain the desired inlet temperature [20]. The schematic diagram of the Pether flow loop can be seen in Figure 2.5.

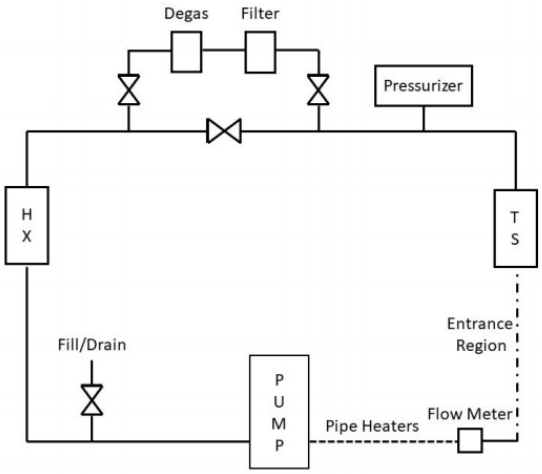

Figure 2.5: Schematic diagram of the Pether Flow Loop [20]

2.2.5 The Flow boiling thermal-hydraulic circuit

The flow boiling thermal-hydraulic circuit at McMaster University was designed to collect steady-state and transient experimental data for CHF. Even though all components have a pressure rating up to 10 MPa at up to 75 K subcooling, according to the authors [7], the experiments run with the pressure range between 2-6 MPa with 1000-2500 kg/m^{2}s. The test section of the loop is connected to 96 kW of DC power. Geometrical information of the test section is provided in Table 2.5 [21]. However, this loop also has restrictions to provide

high-resolution data on prototypical operating conditions.

Table 2.5: Geometrical Information of the McMaster University's test section [7]

Item	**mm**
Length of the test section	1575
Heated length	1321
Inside diameter	4.6
Wall thickness	0.9
Thermocouples location	955, 1113, 1229, 1276, 1293, 1305, 1316

In this facility, the water is circulated by a centrifugal pump controlled by a variable frequency driver (VFD). The pump has a capacity of 8 m^3h^{-1} with a 75 m pressure head at up to 15 MPa. To prevent the pump's damage and have the desired flow rate in the test section, around 80-90 % of the water flows through a bypass line. A bladder accumulator is used to pressurize the system, and it is coupled with its bottom connector 2.28 m above the pump suction line. The steam generated in the test section is condensed with a condensing spray line. Two subcoolers with approximately 43 kW heat removal capacity are located after the condensing spray line. These subcoolers and the condensing spray line are essential to ensure that the downstream piping void fraction is zero and the flow after them is single-phase. In addition, the water coolant should also be at single-phase before the accumulator. After the pump, there is a preheater (128 kW) to adjust the inlet temperature of the test section. Calibrated thermocouples (Omega type K thermocouples) are used to measure the inlet and outlet temperatures of the test section, and a Coriolis mass flow meter has been used to measure the mass inlet flow. An absolute pressure transducer, similar to other loops, measures the outlet pressure drop. A differential pressure transducer is used to measure the

pressure drop of the test section. The schematic of the flow boiling thermal-hydraulic circuit can be seen in Figure 2.6.

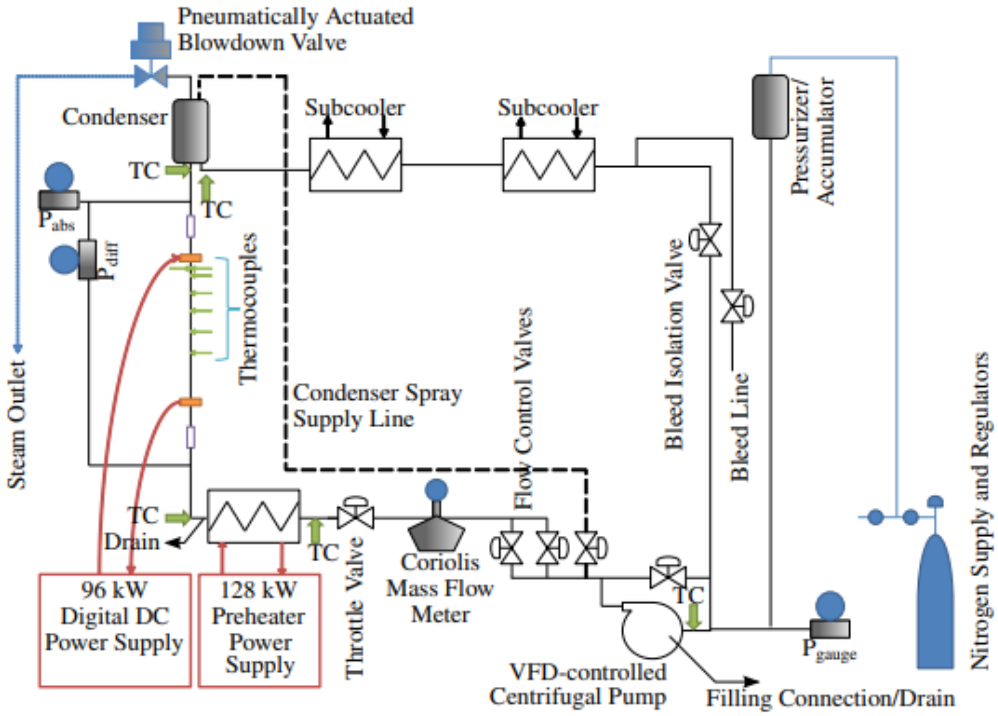

Figure 2.6: Schematic diagram of the Flow Boiling Hydraulic Circuit [21]

The design specifications of the investigated facilities are shown in Table 2.7. These facilities are comprehensive, *i.e.*, there are other facilities in the world. Also, the main components of all of the investigated facilities are shown in Appendix A.1.

#	Institute /Facility	Max pressure [bar]	Max temperature [K]	Max Power [kW]	Max q" [kW/m^2]	Max Mass Flux [kg/m^{2}s]	Heating length [m]	Rod geometry	TC spatial resolution [m]	Working fluid
1	Post-CHF Heat Transfer (PCHT) test facility (Michigan)	34.5	573	34	737.4	2000	1.05	Single tube	0.0065~0.12	Water
2	Reactor coolant system thermal hydraulic loop facility (RCS loop facility)	160	620	470	2882.4	650	3.672	3x3 bundle	0.01~0.4	Water
3	Royal Institute of Technology (KTH), Stockholm, Sweden.	250	613	1000	Vary with TS	1 kg/s*	~ 7.3	Vary	-	Water
4	MIT Flow Boiling Experimental Facility	10	453	5	12000*	2000	0.01	Rectangular ITO	0.000015 (IR resolution)	Water
5	McMaster University Flow boiling thermal-hydraulic circuit	60	478	96	5028.8	2500	1.321	Single tube	0.011~0.157	Water
6	PHILUS (high Pressure HIgh temperature annuLUS flow) Facility	180	630	100	3350.6	3700	1	Single Tube	0.001	Water
7	Pressurized Water Reactor	155.1	600	-	~589.8	3729	-	-	-	Water

Figure 2.7: Summary of Design Specifications of Investigated Flow Boiling Facilities

Only five of the loops around the world have been investigated. Thousands of loops were constructed in the world, and hundreds of loops are designing. The comparison among investigated thermal-hydraulic loops worldwide demonstrates a lack of high-spatial resolution temperature measurement in the test section with the thermocouples. Thermocouples are not capable of measuring the temperature at high spatial resolution. Due to the advancements in distributed optical fiber temperature sensors, a much higher spatial resolution can be obtained for surface temperature measurements. With the help of the high-resolution measurement, the temperature can be measured millimetrically, which decreases the uncertainties. Also, there are not that many loops with a high working temperature, pressure, and mass flux. These are some reasons why the PHILUS is a unique loop. During this chapter, it was shown that the thermal-hydraulic loops use different ways to provide the inlet and the outlet boundary conditions of the test section, and all of them are used to acquire data to improve correlations on CHF and post-CHF. Also, this study reveals that some of the loops are constantly being updated, so this encouraged us to design the PHILUS facility with

flexibility for future upgrades. In the next chapter, the description of the PHILUS facility components is provided.

Chapter 3

Design of the PHILUS

The PHILUS facility employ a directly heated tube and annular flow channel, and it was designed to investigate CHF and post-CHF characteristics at PWR conditions [22]. This chapter discusses the design of the primary and secondary loops. This discussion explains the reasons to select each component and its basic functions. Also, the calculations behind these selections are explained. The PHILUS facility consists of primary and secondary loops. The CAD drawing of the PHILUS facility is shown in Figure 3.1.

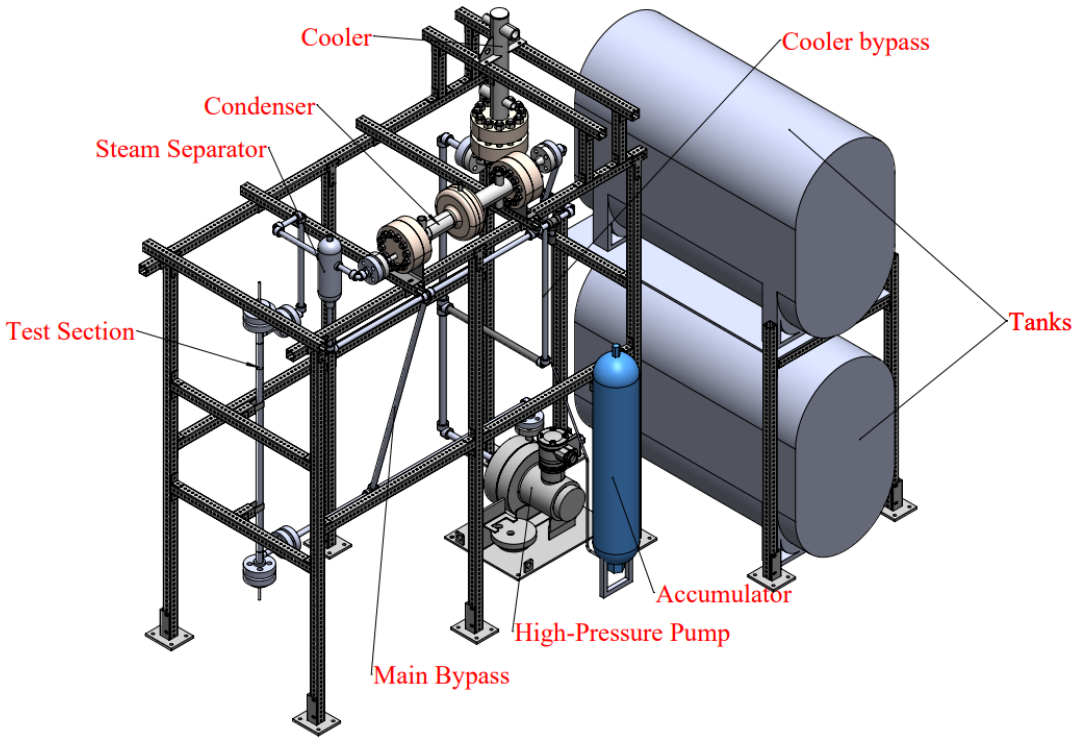

Figure 3.1: The CAD drawing of the PHILUS facility

The primary loop is designed to maintain the inlet and outlet conditions of the test section. The secondary loop is mainly designed to remove the heat generated from the primary loop through the flow of the coolant water in heat exchange components.

3.1 Test section

A schematic of the test section can be seen in Figure 3.2. The flow housing of the test section is 1" sch. 80, SS 316 pipe with a removable 9.5 mm OD heater rod running down the centerline in order to allow for annular flow. The flow dimensions of the test section, namely flow area to power ratio and rod diameter, are designed to mimic that of a pressurized water reactor (PWR) core subchannel shown in Figure 3.3. The rod-to-rod pitch and cladding diameter in the PWR cores are 12.6 mm and 9.5 mm, respectively, and these two numbers are used to define the flow of the PHILUS facility. With these numbers, the flow is of the PHILUS facility is 87.9 mm^2. The total length of the test section is 1320 mm, of which 1000 is the heated length with unheated 130 mm at the top and 190 mm at the bottom to allow for fully developed flow. There are two cooling flanges at the bottom and top of the test section to cool electrodes, power connections, and instrumentation. With the help of the cooling, the lifetime-sensitive components in the test section will be extended. Specification of the test section can be seen in Table 3.2. The maximum designed total power is 100 kW. The test section is operable at up to 22 MPa at 370°C, and is designed in accordance with ASME B31.1. The cladding of the rod is directly heated and filled with Alumina ceramic to provide electrical insulation for instrumentation. The test section has connected to the rest of the loop with 3/4" 2500# flanges.

Two different rods were acquired. Zirconium 702 and Inconel 600 are used for the outer cladding for each of the two heater rods. Material specifications of the rods are shown in

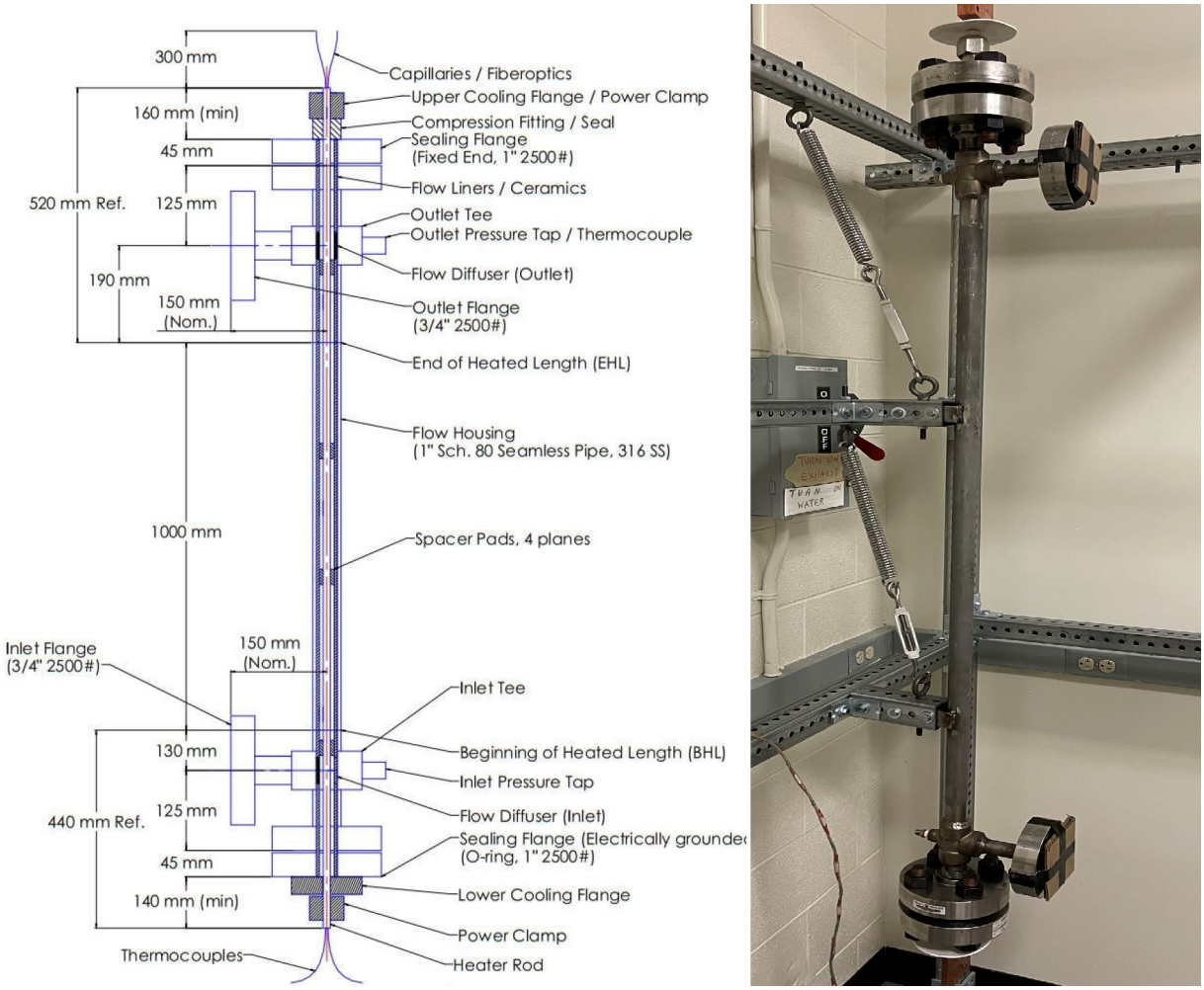

Figure 3.2: (Left) Test Section Schematic and (Right) Photo of the Test Section

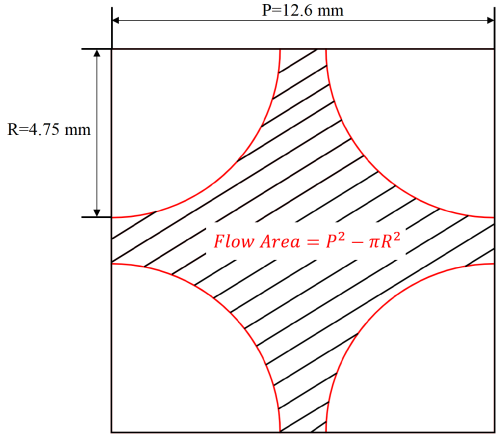

Figure 3.3: PWR Subchannel cross-section [13]

Table 3.1. With these two different material claddings, the effect of these materials on CHF and post-CHF heat transfer can be observed. These materials are the common cladding materials used in heat transfer experiments. The top view of the heater rod can be seen in Figure 3.4. Seven K-type thermocouples are embedded underneath the cladding, with three at equal radial spacing located 10 mm from the top of the heated portion of the test section, two located 50 mm, and two located 100 mm from the top. The specification of the thermocouples is shown in Table 3.3. In addition, three stainless steel capillary tubes are embedded in the ceramic. The capillaries are 304 stainless steel with a 1.07 mm outside diameter and a nominal wall thickness of 0.20 mm. These capillary tubes are designed to allow for the insertion of optical fibers in order to measure temperature along the full heated test section length. Each thermocouple is located at an angle of either 0, 120, or 240 degrees, and the capillary tubes are located at 60, 180, and 300 degrees. Spacer pads in the heater rod are used to help place the heater rod in the center of the flow channel and prevent it from being bent.

Table 3.1: Physical Properties of Zirconium 702 and Inconel 600

Type	**Zirconium 702**	**Inconel 600**
Density (ρ) kg/m^3	6.5	8.43
Melting Point $^\circ C$	1852	1413
Thermal conductivity (k) $W/m^\circ C$	22	14.9
Specific Heat (0-100 $^\circ C$) (c_p) kJ/kgK	0.285	0.444
Thermal effusivity ($\sqrt{\rho k c_p}$) $KJ/\sqrt{s}m^2K$	40.75	55.76

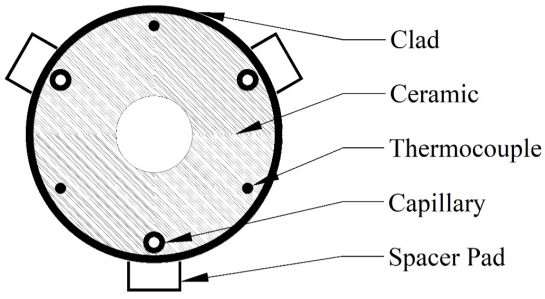

Figure 3.4: Top view of the heater rod

Table 3.2: Specification of the Test Section

		Directly Heated Heater Rod	
		Type 1	**Type 2**
Operational Condition	Clad and Sheath Material	Zirconium 702	Inconel 600
	Max. External Pressure	22 MPa	
	Max. Clad Surface Temperature	$370°C$	
	Total Power	100 kW	
	Max. Linear Power	100 kW/m	
	Max. Surface Heat Flux	335 W/cm^2	
Geometrical Information	Clad Outside Diameter	9.5 mm	9.5 mm
	Wall thickness	0.89 mm	0.89 mm
	Heated Length	1000 mm	
	Top Cold Length	510 mm	
	Bottom Cold Length	385 mm	
	Overall Length	1895 mm	
	Overall Electrode Length	175 mm	

Table 3.3: Specification of the Thermocouple

Thermocouples	**Value**
Type	Premium Grade, Type K
Material	Inconel 600
Insulation Material	MgO
Juction Type	Ungrounded, BN backfilled
Outside Diameter	0.50 mm
Overall Length	3650 mm
Quantity	6 per heater
Capillary Tube Parameter	
Material	304 SS
Outside Diameter	1.07 mm (Nominal)
Wall Thickness	0.20 mm (Nominal)
Overall Length	1750 mm
Quantity	3 per Heater

3.1.1 Optical Fibers

For the purposes of improving temperature measurement resolution, optical fiber temperature sensors are implemented in the test section. Changes in the temperature cause strain in the minor imperfections of each fiber, which slightly alter the scattering of light passing through [23]. The alternation, known as the spectral shift, can be measured with an optical fiber and converted to temperature change by fitting the spectral shift across the optical fiber at numerous locations to known temperature variations. This allows the fibers to measure the inner temperature of the cladding. The optical fiber will allow temperature measurement during CHF experiments at the precise CHF location with an unprecedented high spatial resolution. Differently than thermocouples, which measure the temperature at a single point, optical fibers can measure it at millimetric-scale resolution along the entire heated length. The optical fibers designed by Luna Inc. are operable at up to 600°C. The schematic of the optical fiber is shown in Figure 3.5. The sensing section uses a silica sheath to maintain the structural integrity of the fiber during the experiments. The gauge pitch of the ODiSI 6102 is 0.65 mm with a 31.25 Hz frequency. This specification allows for the measurement of CHF temperature and CHF location under the PHILUS facility working conditions. These measurements are essential to analyze the complex two-phase flow phenomena.

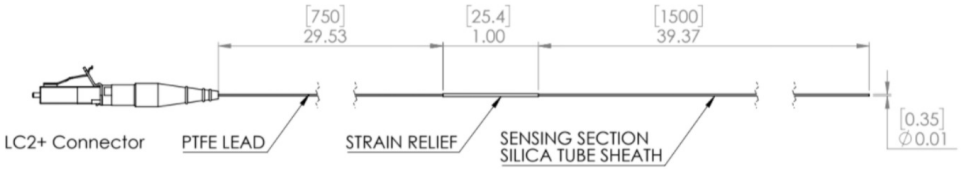

Figure 3.5: Schematic of the Optical Fibers

For -40 to 200°C, the fit from the spectral shift and temperature is linear, while the spectral shift is nonlinear for the higher temperature applications. Thus, the thermocouple's reading

and the optical fiber's measurement will be compared at high temperatures. Calibration between the spectral shift measurements from the optical fibers used in this facility and respective temperature values was performed in a previous study [24], [25].

3.2 Piping

3.2.1 Primary piping

Piping is one of the most critical subjects for designing the loop because it will connect all instruments to work under the design conditions. Following ASME specifications, ¾ inches schedule 160 stainless steel 316/L (Sch 160 SS 316/L) pipes were chosen as the most convenient option for the primary loop because it has the closest flow area to the test section. However, 1" tubes are used between the cooler and the pump because of the suction flange's size. The reason for this will be explained in section 3.5. Schedule (sch) refers to the thickness of the tube.

As it can be seen in Table 3.4, 3/4" sch. 160 pipes have 1.05 inches outside diameter (OD) with 0.218 inches thickness. Fig.3.6 shows the cross-section view of the 3/4" tube.

Table 3.4: ANSI/ ASME B36.10M Standards for thickness

Nominal pipe size inch	**Outside Diameter inch**	**Pipe Schedules Wall thickness (inch)**				
		5	10	40	80	160
1/8	0.405	-	0.035	0.068	0.095	-
1/4	0.54	-	0.049	0.088	0.119	-
3/8	0.675	-	0.049	0.091	0.126	-
1/2	0.84	0.065	0.065	0.109	0.147	0.187
3/4	1.05	0.065	0.065	0.113	0.154	0.218
1	1.315	0.065	0.065	0.133	0.179	0.25
1 1/4	1.66	0.065	0.065	0.14	0.191	0.281
1 1/2	1.9	0.065	0.065	0.145	0.2	0.343
2	2.375	0.065	0.065	0.154	0.218	0.375

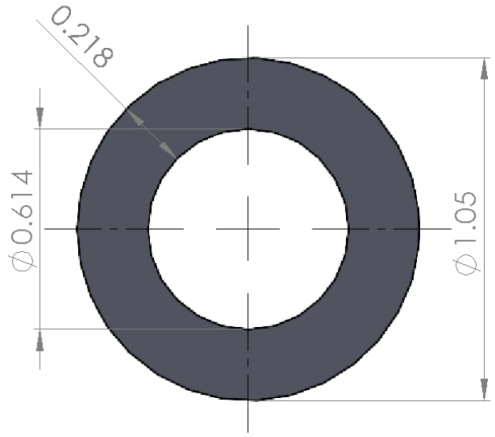

Figure 3.6: Dimensions of 3/4 inches the Sch-160 SS 316/L

Table 3.5 illustrates the working pressure limits depending on temperature. The chosen pipe can work under the PHILUS experimental conditions. After pipe selection, fitting was selected to connect the loop components. Elbows, tees, and flanges are the three essential fittings in the loop. Stainless steel 316/L; 3/4" 6000 # socket weld tees and 90° elbows are used in the primary loop. A side view of the elbow is in Figure 3.7. In Table 3.6, the dimension of the elbow can be seen.

Table 3.5: Working Pressure Between 400-800 Fahrenheit Degrees

				Pressure (PSIG) for 3/4 in					
Temperature (°F)				400	500	600	700	800	850
TYPE	Thickness (in)	OD (in)	Area (mm^2)						
Sch 160 316L	0.218	1.05	191.026	5355	4975	4665	4460	4285	4180

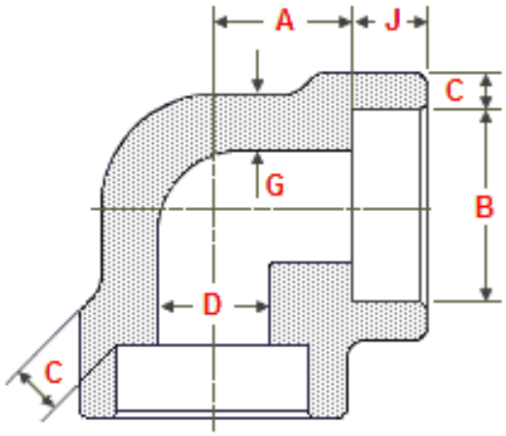

Figure 3.7: Side view of socket weld 90° elbows to ASME B16.11 class 6000

Table 3.6: Dimensions of socket weld 90 elbows to ASME B16.11 class 6000

NPS		**Socket Bore Dia. (B) (mm)**		**Fitting Bore Dia. (D) (mm)**		**Socket Wall Thickness (C) (mm)**		**Body Wall Thickness (G) (mm)**	**Socket Depth (J) (mm)**	**Center to Bottom of Socket (A) (mm)**
(inches)	(mm)	Min.	Max.	Min.	Max.	Avg.	Min.	Min.	Min.	-
¾	19.05	27.05	27.3	14.8	16.3	6.95	6.05	5.55	13	22.5
1	25.4	33.80	34.05	19.9	21.5	6.95	7.90	6.35	13	27

Instruments and pipes can be connected with flanges, hubs, and clamps. Table 3.7 shows the features of the connection types.

Table 3.7: Comparison of the Flanges, Hubs, and Clamps

	Flanges	**Hubs and Clamp**
Tension **Bending** **Compression**	Weakest link in the piping system therefore can cause leakage	Withstand greater load and stress than the piping system itself ultimately provide better tightness
Seal **gasket**	Gasket must be replaced during maintenance	Self-energized metal seal ring can be reused
Installation **arrangement**	Bolt holes must be aligned Multiple bolts (up to 24) Longer overall length Larger overall diameter Flange connection takes time to be assembled or disassembled	No bolt holes to align 4 bolts to tighten Shorter overall length Smaller overall diameter Quicker assembled or disassembled
Spares	Traditional sparing management must be considered	Sparing is significantly reduced
Manufacture **Standards**	Multiple sizes are widely available in the industry and made by many manufacturers	Limited manufacturers not standardized among manufacturers
Design	Industry standard	Need careful study and selection to choose the right hubs clamp for its intended purpose

There are a couple of reasons to choose flanges. Some of them are consistency, price, and standardization. Sternlabs designed the test section with flanges at the inlet and outlet. Also, flanges are cheaper than hubs. More importantly, it has industrial standards. Therefore, 2500 # raised face socket weld Sch 160 bore flanges are used as flanges. A side view of the flanges can be seen in Fig. 3.8. Table 3.8 shows the dimension of the flanges.

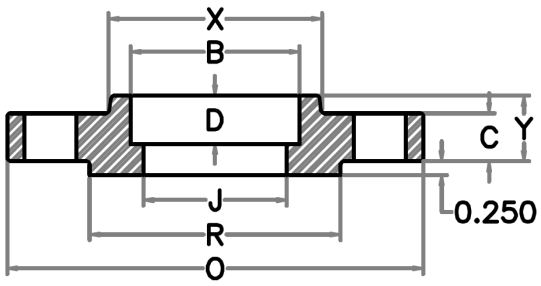

Figure 3.8: Side view of 2500 # raised face socket weld sch 160 bore flange

Table 3.8: Dimensions of 2500 # raised face socket weld Sch 160 bore flanges

inch								
Nominal Pipe Size	Outside Diameter of Flange (O)	Thickness of Flange Min. (C)	Diameter of Raised Face (R)	Diameter of Hub at Base (X)	Threaded Slip-On Socket Welding (Y)	Slip-On Socket Welding Min. (B)	Welding Neck Socket Welding (J)	Depth of Socket (D)
3/4	5.50	1.25	1.69	2.00	1.69	1.09	*	0.44
1	6.25	1.38	2.00	2.25	1.88	1.36	*	0.50

3.3 Steam Separator

The steam separator is an essential component of the two-phase flow loop. The main purpose of the steam separator is separate the vapor and liquid of water. Therefore, after the test section outlet, the flow is directed to the steam separator. In the steam separator, separated vapor condense via the condenser while the liquid water flows through the main bypass line. With the condenser and the steam separator, the vapor flow will be restricted in these two components, and it helps to minimize the accumulator volume, as discussed in Section 3.6. The design and working parameters of the steam separator can be seen in Table 3.9.

Table 3.9: Design and Working Parameters of the Steam Separator

	Design Condition	**Working Condition**
Pressure (MPa/PSI)	19.30/2800	18/2610
Temperature $(°C/F)$	371.11/700	350/662
Steam Flow Rate $((kg/s)/(lbs/hr))$	0.1123/891	

The inlet of the steam separator is connected above to the outlet of the test section. The water vapor density is much lighter than the liquid water, and these differences separate the

liquid to vapor. Schematic of the steam separator is shown in Figure 3.9 where A, B, C, and D are vent, inlet, outlet, and drain, respectively.

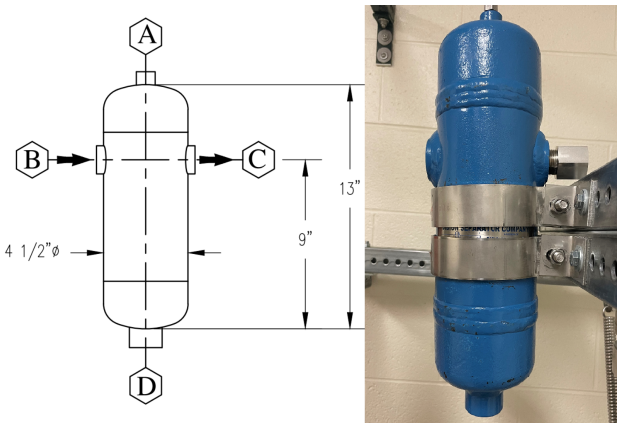

Figure 3.9: (Left) Schematic of the Steam Separator and (Right) Picture of the Steam Separator

The steam mass flow rate was calculated with Eq. 3.1. Maximum power has been used in the calculation to ensure the steam separator is enough to separate all the possible steam that can be generated within the system.

$$\dot{m}_{steam} = \frac{\dot{q}_{max}}{h_{fg}} \tag{3.1}$$

Equation 3.1 shows that the maximum mass flow rate of the steam ($\dot{m}_{steam}$) is the ratio of the power ($\dot{q}_{max}$) and latent heat (h_{fg}).

3.4 Heat Exchange components

There are two places where heat is removed. One of them is a single-phase cooler with a capacity to remove up to 100 kW (the test section's maximum power). The other is the condenser with a capacity of approximately 50 kW, depending on the operating pressure

and mass flux.

3.4.1 Condenser

The condenser is located between the pressurizer and the steam separator. The vapor can be condense only in the condenser. After the steam separator, the water vapor flows into the condenser and exits it as liquid water. Photo and schematic of the condenser are shown in Figure 3.10

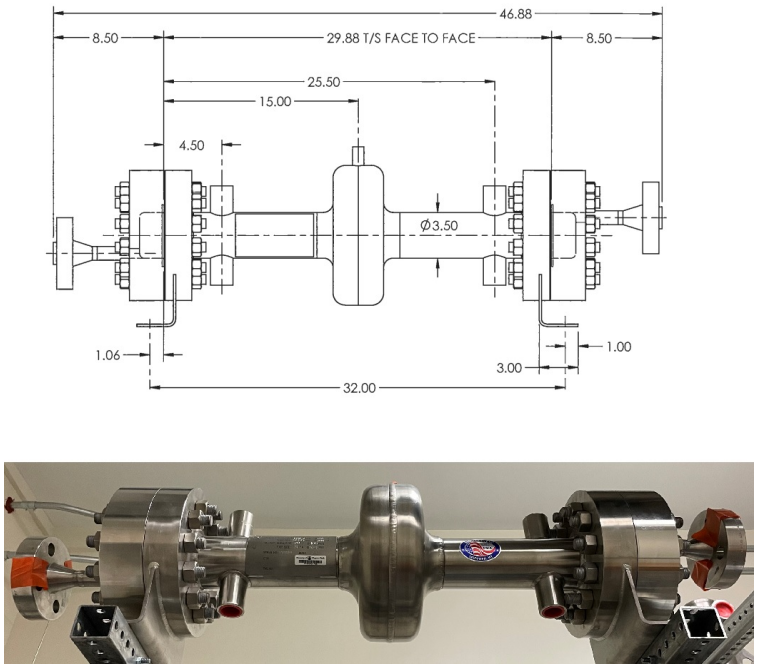

Figure 3.10: (Top) Schematic of the Condenser and (Bottom) Picture of the Condenser

In Table 3.10, the nominal flow rate with the minimum pressure at saturation temperature shows the maximum necessary heat removal to reach liquid water. TRACE was used the simulate the test section to calculate the quality at the CHF conditions because the capacity of the heat exchangers is determined at CHF conditions, energy balance calculation is not enough. TRACE (TRAC/RELAP Advanced Computational Engine) is a thermal-hydraulic

Table 3.10: Test conditions and TRACE predictions for determining heat removal requirements (courtesy from Paul Hurley)

Input	**Mass Flux** ($kg/m^2.s$)	3700	3700	3700	3700	500	500	500	500	500	500	500
	Total Power (kW)	96	58	77	51	28	43	19	39	27	46	17
	Outlet Pressure post-CHF (MPa)	15.5	15.5	7	19	15.5	15.5	15.5	7	7	19	19
	Inlet Temp ($°C$)	292	344	285	361	292	200	344	200	285	200	361
Output	**Outlet Quality**	0.004	0.113	0.104	0.131	0.311	0.203	0.437	0.313	0.403	0.178	0.546
	Outlet Enthalpy (h_{outlet})	1602	1704	1406	1796	1929	1825	2051	1736	1871	1870	2156
	Enthalpy Differences Between Outlet and Liquid Water (kj/kg) (Δh)	4	117	156	114	299	196	422	472	608	138	425
	Power of the Condenser (kW) ($\dot{Q}$)	1.32	38.23	51.75	37.25	13.17	8.62	18.58	20.75	26.75	6.09	18.72

code developed by the U.S Nuclear Regulatory Commission [12]. The qualities are used to calculate the capacity of the cooler and the condenser. To calculate the necessary heat, the following equations are applied.

The outlet enthalpy of the test section can be calculated using Eq. 3.2.

$$h_{outlet} = x \times h_g + (1 - x) h_f \tag{3.2}$$

After calculating the outlet enthalpy, Eq. 3.3 can be used for calculating the enthalpy difference between the outlet and the liquid fluid.

$$\Delta h = h_f - h_{outlet} \tag{3.3}$$

With this enthalpy difference, required power differences can be calculated using Eq. 3.4. This provides the total necessary power to condense the total vapor generated in the test section.

$$\dot{Q}_{Cond.} = \dot{m} \times \Delta h \tag{3.4}$$

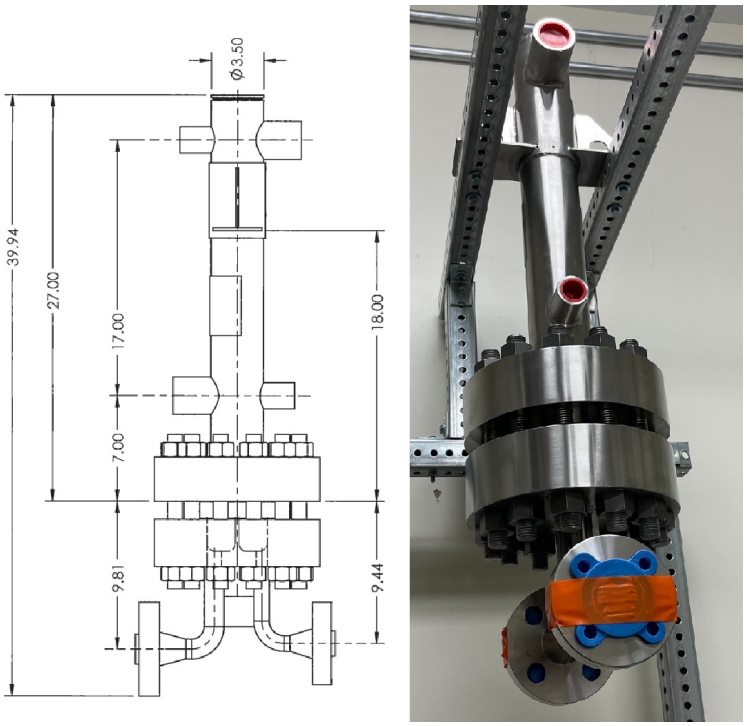

Figure 3.11: (Left) Schematic of the Cooler and (Right) Picture of the Cooler

3.4.2 Cooler

The cooler is located between the pressurizer and the pump. The picture and schematic of the cooler are shown in Figure 3.11 The primary purpose of the cooler is to cool the single-phase water to the required inlet temperature. Since the loop is working in various conditions, the CHF occurs at different pressures and given power. In order to calculate the required heat transfer of the cooler, the following steps apply TRACE simulation data,

$$\dot{Q}_{Cooler} = Total\ Power - \dot{Q}_{Cond.} \tag{3.5}$$

If the flow is single-phase after the maximum design power (100 kW) in the test section, the flow cannot be directed to the condenser, so the cooler is the only heat exchange component. Because of that, the cooler is designed to remove the maximum design power of the test

section (100 kW).

3.4.3 Calculation of Required Heat Transfer Surface

The total heat transfer surface (S) for the cooler and the condenser components can be calculated with Eq. 3.6. To calculate it, the power ($\dot{Q}$), overall heat transfer coefficient (H), the logarithmic mean temperature difference for counter-flow arrangement (Δ T_{LM}), and a correction factor (F) should be known.

$$S = \frac{\dot{Q}}{H \Delta T_{LM} F} \tag{3.6}$$

In order to calculate the heat transfer rate in a cooler (single-phase-liquid), Eq. 3.7 can be used. Mass flow rate at the shell side (m_s), mass flow rate at the tube side (m_t), specific heat shell and tube side ($C_{p_{st}}$), and inlet and outlet temperature of the shell and tube side (T_{st}) should be known.

$$\dot{Q} = \dot{m}_s C_{p_s} (T_{o_s} - T_{i_s}) = \dot{m}_t C_{p_t} (T_{i_t} - T_{o_t}) \tag{3.7}$$

Heat transfer rate calculation in two-phase flow is explained in Subsection 3.4.1.

To calculate the overall heat transfer coefficient with Eq. 3.8, the shell side and the tube side heat transfer coefficient should be known.

$$\frac{1}{H} = \frac{1}{h_s} \times \frac{1}{h_t} \tag{3.8}$$

The logarithmic mean temperature difference for counter-flow arrangement can be calculated

with the same parameters that are provided in Eq. 3.9.

$$\Delta T_{LM} = \frac{(T_{i_t} - T_{o_s}) - (T_{o_t} - T_{i_s})}{\ln \frac{T_{i_t} - T_{os}}{T_{o_t} - T_{i_s}}} \tag{3.9}$$

The required surface for any heat exchanger can be calculated with all this information. However, the two missing values for us are the correction factor and the heat transfer coefficient for both the shell and tube sides.

To provide F, Eq. 3.10 [26] needs to be calculated.

$$F = \sqrt{\frac{R^2 - 1}{R - 1}} \times \frac{\ln(1 - P) \times (1 - (P \times R))}{\ln \frac{2 - (P \times R) + 1 - \sqrt{R^2 + 1}}{2 - (P \times R) + 1 + \sqrt{R^2 + 1}}} \tag{3.10}$$

Correction coefficient (R) and Efficiency (P) can be found with Eq. 3.11 and Eq. 3.12.

$$R = \frac{T_{t_i} - T_{t_o}}{T_{s_o} - T_{s_i}} \tag{3.11}$$

$$P = \frac{T_{s_o} - T_{s_i}}{T_{t_o} - T_{s_i}} \tag{3.12}$$

or it is easier to calculate with Figure 3.12

In order to calculate the tube side heat transfer coefficient, the Reynolds number and the Prandtl number of the flow in the tube side should be known. For Reynolds numbers larger than ten thousand, Eq. 3.13 [27] can be used.

Tube side heat transfer coefficient:

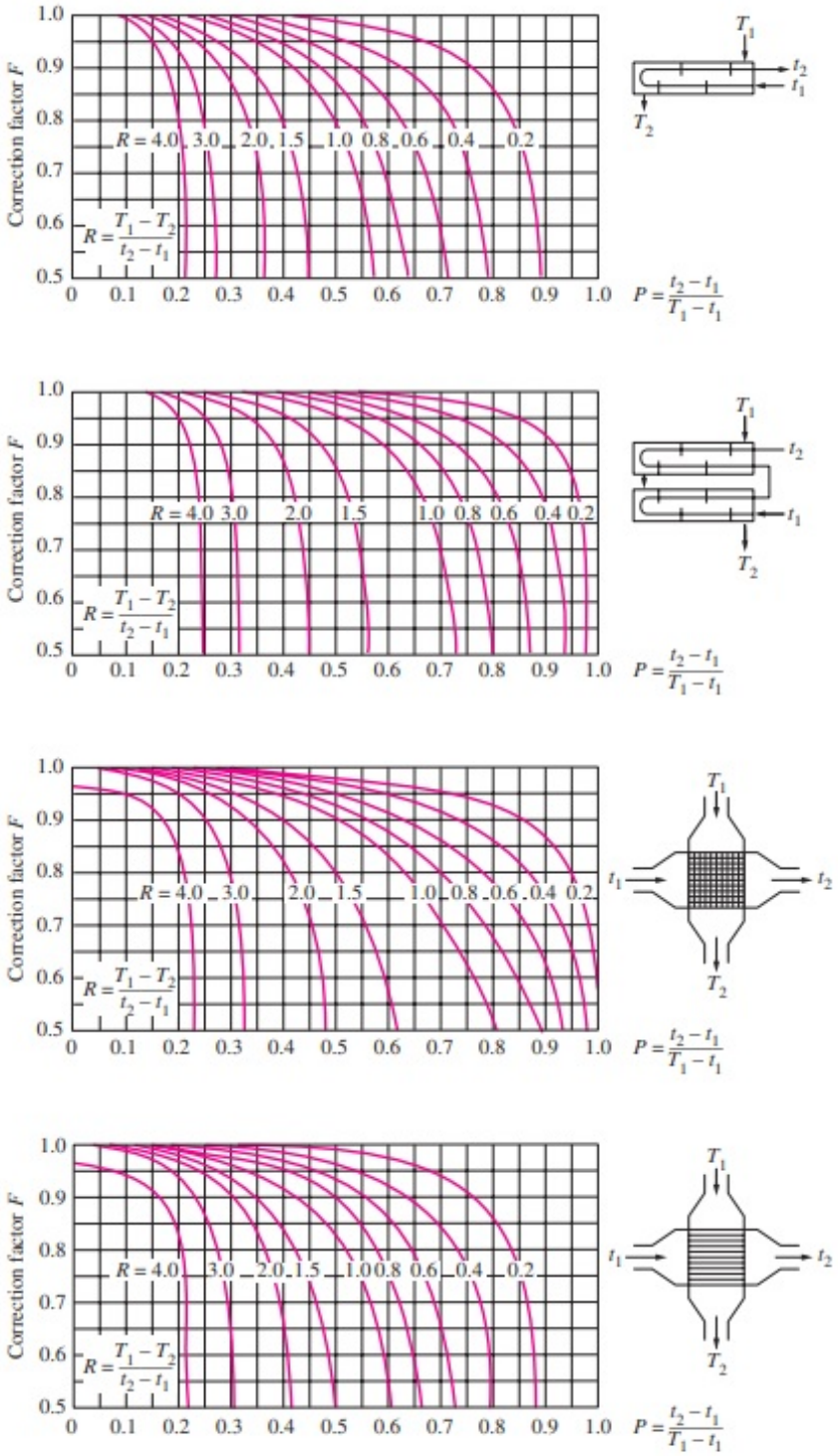

Figure 3.12: Correction factor for different flow types

$$h_t = 0.027 \times \frac{k_t}{d_o} \times {Re_t}^{0.8} \times {Pr_t}^{1/3} \times \left(\frac{\mu_t}{\mu_{wt}}\right)^{0.14} \tag{3.13}$$

Reynolds numbers can be calculated with Eq. 3.14. To calculate the Reynolds number, velocity of the tube side should be known. Velocity can be calculated with Eq. 3.15

where, μ and d are the dynamic viscosity and diameter of the tube, respectively. Subscription o and i represent outer and inlet, respectively.

$$Re_t = \frac{\rho \times v_t \times d_i}{\mu_t} \tag{3.14}$$

$$v_t = \frac{m_t}{\rho_t \times A_{tube} \times N} \tag{3.15}$$

where, m_t is the mass flow of the tube side, ρ_t is the density of the water on the tube side, A_{tube} is the flow area of each tube, and N is the number of tubes in the shell side.

Prandtl number can be calculated with Eq. 3.16.

$$Pr_t = \frac{(\mu_t \times c_{p_t})}{k_t} \tag{3.16}$$

where, μ_t is the tube sides viscosity of the water, k_t is the thermal conductivity, c_{p_t} is the specific heat capacity at constant pressure at the tube side.

The shell side heat transfer coefficient [27]:

$$h_s = \frac{j_i C_{ps} v_s {\phi_s}^n}{Pr_s^{2/3}} \tag{3.17}$$

where j_i and ${\phi_s}^n$;

$$j_i = 1.73 \times Re_s^{(-0.694)} \qquad 1 \leq Re_s < 100 \tag{3.18a}$$

$$j_i = 0.717 \times Re_s^{(-0.574)} \qquad 100 \leq Re_s < 1000 \tag{3.18b}$$

$$j_i = 0.236 \times Re_s^{(-0.236)} \qquad 1000 \leq Re_s \tag{3.18c}$$

$${\phi_s}^n = \left(\frac{\mu_t}{\mu_{wt}}\right)^{0.14} \tag{3.19}$$

where, μ_s is the bulk mean temperature of the fluid and μ_w is the viscosity gradient at the tube wall.

and,

$$Pr_s = \frac{\mu_s \times C_{ps}}{k_s} \tag{3.20}$$

The required specification of cooler calculated by hand is shown in Table 3.11. The two main reasons for the error are baffle and cleaning. Baffles increase the heat transfer rate while the dirt decreases it. During the calculation, these effects are neglected, so the error is more than 25%.

Table 3.11: Hand Calculated Specification of the Cooler

Component	**Heat Exchanged (kW)**	**Logarithmic Mean Temperature Differences** ($^\circ C$)	**Overall Heat Transfer Coefficient** ($kW/m^2.^\circ C$)	**Correction factor**	**Surface** (m^2)	**Error** (%)
Cooler	100	280.53	1.513	0.98	0.240	-25.65

With all these calculations, Enerquip LLC. manufactured the cooler and the condenser for the loop. The required heat transfer surface calculation of the manufactured cooler and condenser is shown in Table 3.12. Some of the specifications can also be seen in Table 3.13.

Table 3.12: Required Heat Transfer Surface

Components	**Heat Exchanged (kW)**	**Logarithmic Mean Temperature Differences** ($°C$)	**Overall Heat Transfer Coefficient** ($kW/m^2.°C$)	**Correction factor**	**Surface** (m^2)
Cooler	100	298.296	1.801	0.975	0.191
Condenser	52	257.965	0.879	0.97	0.236

Table 3.13: Specification of the Heat Exchange Components

	Cooler		**Condenser**	
(In/Out)	Shell side	Tube Side	Shell side	Tube Side
Type	BEU (Vertical)		BEM (Horizontal)	
Viscosity (cP)	1.0016/0.979	0.0666/0.0875	1.0016/0.6679	0.0190/0.0912
Specific Heat (kJ/Kg-$°C$)	4.191/4.181	11.505/5.496	4.187/4.181	5.357/5.404
Thermal Conductivity (W/m-$°C$)	0.5993/0.625	0.431/0.555	0.599/0.626	0.0643/0.568
Velocity	0.618744	1.7708	0.3048	0.4633
Design Pressure (kPa)	689.476	18,615.84	689.476	18,615.84
Design Temperature ($°C$)	65.55	371	65.55	371

In the 3rd row of Table 3.13, the type of the heat exchanger can be seen. B, E, U, and M letters indicate the bonnet (integral cover), one-pass shell, U-tube bundle, and fixed tube sheet, respectively.

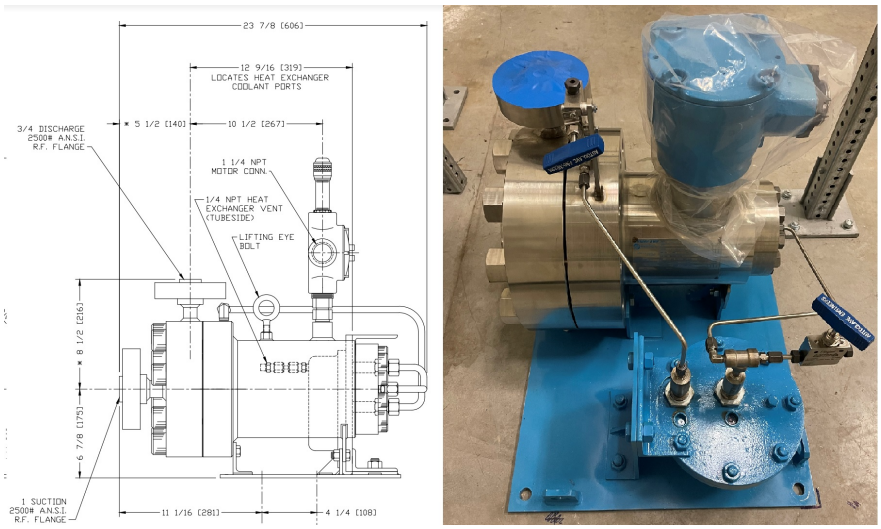

Figure 3.13: (Left) Schematic of the High-Pressure Pump and (Right) Picture of the High-Pressure Pump

3.5 High Pressure pump

A custom design Teikoku GBT-1.5K-278 centrifugal pump was chosen for the high-pressure pump. The schematic and picture of the high-pressure pump are shown in Figure 3.13. Operation conditions of the pump are 7.5 to 50 GPM at $350°C$ and 18 MPa. The high-pressure pump is used to provide coolant water to the heated test section. After the test section heats the coolant, there is a two-phase flow in the outlet of the test section. The flow is separated by a steam separator that is explained in section 3.3. The pressure drop of the loop is significant, and to compensate this pressure drop, the pump head is 150 ft. The required net positive suction head (NPSH) of the pump is 2.84 ft, and available NPSH can be calculated with Eq. 3.21. Also, the pump connects to the loop with flanges, and the suction flange (1 in, 2500#RF) is larger than the discharge flange (3/4 in, 2500#RF). This is to minimize the resistance on the suction side, reduce the friction loss, and increase the NPSH.

Table 3.14: Specification of the Pump

Parameter	Value	Parameter	Value	Parameter	Value
Design Pressure (psi)	2700	Impeller Diameter (in)	5.00-6.50	Flow rate (GPM)	7.5-50
Suction Flange Size (in)	1	Design Differential Head (ft)	150.6	Maximum Temperature (F)	700
Discharge Flange Size (in)	0.75	Required Differential Head (ft)	150	NPSH (ft)	2.84

$$NPSH = \left(\frac{P_i}{\rho g} + \frac{V_i^2}{2g}\right) - \frac{P_v}{\rho g} \tag{3.21}$$

where, P_i : absolute pressure at the inlet V_i : average velocity at the inlet ρ : fluid density g : acceleration of gravity P_v : vapor pressure of the fluid

The pump's main specifications can be seen in Table 3.14. The pump is connected to a variable frequency drive (VFD) controller, a type of motor controller that drives an electric motor by varying the frequency and voltage of its power supply. In that way, the flow rate of the high-pressure pump can be controlled. A Danfoss FC202 VLT Aqua Drive has been chosen as a VFD.

The pump head is a measurement of the pressure drop transformed into height units representing the total pressure required to pump the water to that height. Pressure drop occurs due to friction, gravity, and acceleration. For single-phase steady-state flow in a closed loop, the pressure drop is mainly due to wall friction in each component. Then, the single-phase pressure drop can be calculated using Eq. 3.22.

$$\Delta P_{friction} = f \times \frac{L}{D} \times \frac{\rho V^2}{2} \tag{3.22}$$

where f, L, D, V, and ρ, represent Darcy friction factor, pipe length, pipe diameter, fluid density, and fluid velocity, respectively.

To determine the friction factor, Reynolds's number should be known,

$$Re = \frac{D \times V \times \rho}{\mu} \tag{3.23}$$

The flow is in the laminar region when $Re < 2100$, and the friction factor can be calculated with Eq. 3.24.

$$f = \frac{64}{Re} \tag{3.24}$$

When $Re > 4000$, flow is turbulent, and friction factor can be obtained by solving Colebrook White Eq. 3.25 [28].

$$\frac{1}{\sqrt{f}} = -2 \times \left(\frac{\varepsilon}{3.7 \times D} + \frac{2.51}{Re \times \sqrt{f}} \right) \tag{3.25}$$

where ε is pipe roughness.

For $2100 < Re < 4000$, the flow is in the critical zone that has no definite friction factor. Churchill Eq. 3.26, 3.27, 3.28 [28] predicts friction factor for the entire flow regime from laminar to turbulent, and it can be used to get an estimate for friction factor in this zone.

$$f = 8 \times \left(\left(\frac{8}{Re} \right)^{12} + (A + B)^{-1.5} \right)^{\frac{1}{12}} \tag{3.26}$$

where,

$$A = \left(2.457 \times \ln \left(\left(\frac{7}{Re} \right)^{0.9} + \left(0.27 \times \frac{\varepsilon}{D} \right) \right)^{-1} \right)^{16} \tag{3.27}$$

$$B = \left(\frac{37530}{Re}\right)^{16} \tag{3.28}$$

These equations are applicable to a single-phase flow. For two-phase flow, one of the most common methods to calculate pressure drop is the Lockhart-Martinelli multiplier [13]. There are two main assumptions during this approach:

1-The single-phase pressure drop relations can be applied to each of the phases in the two-phase flow field.

2-The pressure gradients of the two phases are equal at any axial position.

The pressure drop by gravity can be calculated with Eq. 3.29.

$$\Delta P_{gravity} = \rho \times g \times \Delta H \tag{3.29}$$

where ΔH (m) is vertical elevation or drop, ρ $(^{kg}/_{m^3})$ is the density of the water, and g $(^{m}/_{s^2})$ is the acceleration of the gravity.

The pressure drop in single-phase by acceleration can be calculated with Eq. 3.30.

$$\Delta P_{acc} = \frac{\dot{m}^2}{2 \times \rho} \times \left(\frac{1}{{A_N}^2} - \frac{1}{{A_1}^2}\right) \tag{3.30}$$

where A is the flow area.

The PHILUS is a two-phase loop. TRACE simulations were used by Paul Hurley to determine the required total pressure drop in the loop. The results of TRACE are shown in Table 3.15. Pressure change in the loop is calculated by the change in the pump's inlet and outlet. With this change, the pressure drop can be converted to the pressure head with Equation

3.31. All the simulations in Table 3.15 run at 18 MPa at 0 sub-cooled with various mass fluxes. The purpose of the mass flux variety in the simulation is to reach the desired mass flux in the test section with minimum pressure drop. Also, there is the main bypass line with the bypass valve between the outlet of the high-pressure pump and the inlet of the test section. The main bypass line is necessary to run the pump at a very low flow rate and have a lower total pressure head with a maximum flow rate. With the help of the bypass line, the serviceable pressure head is calculated to be 150 feet in the PHILUS. Maximum expected pressure drop in the PHILUS is at 18 MPa with 3700 $^{kg}/_{m^2 s}$. The total pressure head in this condition is 82.089 ft when the bypass valve is closed, and it is assumed that it will be doubled when the test section is heated.

Table 3.15: Total pressure head simulation in unheated test section in TRACE simulation

Test No	**Test Section Mass Flux** ($^{kg}/_{m^2 s}$)	**Valve Flow Area Fraction**	**Pump Flow Rate (GPM)**	**Total Pressure Head (ft)**
1	500	1.0 (OPEN)	6.09	3.691
2	500	0.2	4.72	2.743
3	500	0.1	2.92	2.079
4	500	0.0 (CLOSED)	1.16	1.519
5	3700	1.0	45.07	197.227
6	3700	0.2	34.91	144.526
7	3700	0.1	21.64	103.257
8	3700	0.0	8.58	82.089

$$h = \frac{\Delta P}{\rho g} \tag{3.31}$$

where ρ is density of water at the outlet pressure, ΔP is the pressure drop (Pa), and g is acceleration of gravity.

3.6 Accumulator

The accumulator is anotComparisonher essential component of the high-pressure facility because it is one of the easiest ways to cope with pressure oscillation and expansion of the water due to the phase change and pressure change. Since pressure affects the critical heat flux behavior, it is essential to have a smooth pressure during the duration of each experiment, especially at the outlet of the test section. There are different types of accumulators. Two of them are bladder and piston accumulators, which are more suitable for high pressure and temperature application.

Since the loop is a closed system, controlling pressure at one point can affect the rest of the loop. The working principle of accumulators is the same. Depending on the accumulator type, a composite bottle or metal needs to be fitted with expandable bladders or a piston. The piston or the bladder store pressurized gas and separate the gas from the fluid in the loop. A charging valve is connected to the top of the accumulators. There are springs and a poppet at the bottom of the bladder accumulators. The piston accumulators have a piston to regulate the volume of the accumulator. The hydraulic cap at the bottom of both accumulators has been used to connect the accumulators to the loop. A cross-sectional view of the accumulators can be seen in Figure 3.14.

Because of the pressure rate, size, and cost, a bladder type accumulator was chosen. A bladder type of accumulator is used in the system to control the pressure and have flexible volume for the thermal expansion. The expansion of the water from liquid vapor should be calculated to determine the volume of the accumulator. During this calculation, Table 3.10

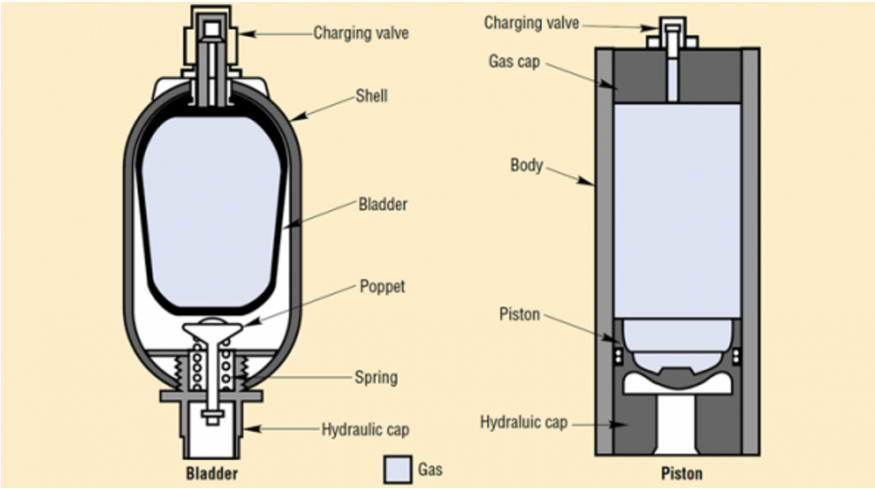

Figure 3.14: Cross-sectional view of the accumulators

is used to calculate the volumetric flow fraction and the expansion of the liquid water from atmospheric pressure to the test pressure that provides the highest outlet quality *i.e.*, the highest volume expansion. Table 3.10 results were used for our lowest design pressure of 7 MPa.

Volumetric flow fraction can be calculated with Equation 3.32,

$$\beta = \frac{1}{1 + [(1-x)/(x)](\rho_v/\rho_l)} \tag{3.32}$$

and,

$$\beta = \frac{V_v}{V_{total}} \tag{3.33}$$

The total volume V_{total} is the volume of the test section, steam separator, condenser, and piping because these are the only locations where the vapor will exist. From this equality, the volume of the vapor (V_v) can be calculated.

Also, volume change in the liquid water needs to be calculated. Temperature change in the liquid water causes a change in the volume of the liquid water. This needs to be carefully calculated because most of the flow in the loop is liquid water.

During this calculation, it is crucial to use the total volume of the loop because the pressure will increase at every location.

Equation 3.34 provide the total mass of water in the loop (m_{total}) at atmospheric pressure. The water mass of the loop will be constant because of the conservation of the mass. The mass of the liquid will change because of evaporation. The final liquid mass (m_{final}) can be calculated with Equation 3.35.

$$m_{total} = V_{loop} \times \rho_{f_{P_{atmospheric}}} \tag{3.34}$$

$$m_{final} = m_{total} - ((V_v) \times \rho_{v_{P_s}}) \tag{3.35}$$

where, $\rho_{v_{P_s}}$ and $\rho_{f_{P_s}}$ is the density of the vapor and liquid water at outlet pressure, respectively.

Volume of the liquid side at any outlet pressure can be calculated with Eq. 3.36. Thus, the volume of the two-phase mixture at any pressure of the loop (V_{new}) can be calculated using Equation 3.37.

$$V_{new} = \frac{m_{final}}{\rho_{f_{P_s}}} \tag{3.36}$$

Finally, change of the volume should be ΔV,

$$\Delta V = (V_{new} - V_{loop}) + V_v \tag{3.37}$$

ΔV is the total expansion volume in the loop, yet it is not the accumulator volume because the accumulator needs to have enough volume to insert nitrogen during the experiment. Also, the accumulator will be filled with some amount of water before starting pressurizing. So, ΔV is around 50% of the accumulator. The specifications of the chosen accumulator are shown in Table 3.16.

Table 3.16: Specification of the Accumulator

Parameters	**Value**
Item Type	Bladder
Item No	RAS-10-C3B08NXW1
Design Pressure (psi)	3000
Allowable Operating Temperature (F)	-20 to 200
Volume (Gallon)	10
Connection	1/4 NPT

Because of the Bladder material, the maximum working temperature of the accumulator is $200°C$. A cooler system is necessary to add between the loop and the accumulator to cool the flow before entering the accumulator. Also, the pressure in the accumulator will be controlled by nitrogen (N_2) pressure using automated fill and relief valves to maintain desired pressure set point during an experiment.

3.7 Valves

A lift check valve is located between the liquid outlet of the steam separator and the bypass outlet to prevent flow from going to the outlet of the steam separator. The flow from the main bypass line needs to be directed because of the pressure drop. Because of that, a lift check valve has been used as a one-way valve. The specification of the lift check valve is in Table 3.17.

Table 3.17: Specification of the Lift Check Valve

Item	**Value**
Name	Swagelok SS-58S12
Connection size (in)	3/4
CV (Flow Coefficient) Maximum	2.2
ASME Class	2500
Working Temperature ($°C$)	Up to 482
Working Pressure (bar)	Up to 413
Equivalent pressure for 370 $°C$ (bar)	248

From Table 3.17, flow Coefficient is the number of gallons per minute of water that will pass through a given orifice area at a pressure drop of 1 psi.

A two-way straight valve is used to fill the loop with water. The filling valve is located at the bottom of the loop. Specification of the globe valve is in Table 3.18.

Table 3.18: Specification of the filling valve

Item	**Two Way Straight Valve**
Item No	20-11LF4-HT
Tube Size	1/4 in
Working Temperature	Up to 1200 $°F$
Working Pressure	Up to 20000 psi
CV (Flow Coefficient) Maximum	0.17

Another essential valve for the high-pressure facility is the relief valve. The relief valve is the safety valve to prevent maximum pressure of the facility from its limits. Every component in the facility has a pressure limit to work. Exceeding this limit can be catastrophic because the components will be damaged to a point where it is impossible to use or cause a safety problem near the facility. To prevent these events, the relief valve needs to set the maximum pressure limit to fail and connect the location where the maximum pressure can be in the facility. A 1/4" R3A series relief valve is used in the system. The set pressure of the relief valve is 3190 psig ($\sim 22MPa$).

3.8 Data acquisition system

LabView was chosen for data acquisition and controlling the parameters. During this section, the specification of the data acquisition system (DAQ system) hardware and controlled parameters are discussed.

3.8.1 DAQ system hardware

National Instruments (NI) Compact cRIO-9045 will be used to collect the data coming from the instruments. The specification of the c-RIO 9045 is in Table 3.19. The NI 9236 350ohm, 8-Ch, 24-Bit, 1/4 Bridge Input Module is used for the pressure transducers. The NI 9213 Spring, 16-ch TC, 24-bit, 75 S/s AI module is for the thermocouples. The NI 9871 4-Port RS422/RS485 Serial Module is to connect to the pumps. The low-pressure pump and the high-pressure pump will be controlled with the NI 9871. Both pumps need to be controlled with the RS485 module. Mass flow rate, pressure, and temperature are the system's boundary conditions, so it is essential to measure them in a critical location, such as the inlet and outlet of the test section or inlet of the high-pressure pump. Also, controlling the low-pressure pump helps steady the temperature across the loop. Thus, these modules that are shown in Table 3.20 are essential components of the DAQ system.

Table 3.19: cRIO module specification

Model	**cRIO-9045**
Channels	8
Working temperature range $°C$	-20 to 50
CPU frequency (GHz)	1.3
Supported operating system	NI Linux Real-Time (64-bit)
Application software	LabVIEW, C/C++ Development Tools for NI Linux Real-Time
Timing accuracy	50 ppm of sample rate

Table 3.20: Modules and purpose

Modules	**Used for**
NI 9236 350ohm, 8-Ch, 24-Bit, 1/4 Bridge Input	The pressure transducers
NI 9213 Spring, 16-ch TC, 24-bit, 75 S/s AI	The thermocouples
NI 9871 4-Port RS422/RS485 Serial	The pumps

Necessary specifications of the NI 9213 spring and NI 9236 350-ohm modules are in Table 3.21.

Table 3.21: Modules and specifications

Model	**NI 9213 Spring**	**NI 9236 350-ohm**
Channels	16	8
Measurement Range	78.125 mV	
Gain Error (High-resolution/High speed)	0.07%/0.08%	
Maximum Gain Error (Calibrated/Uncalibrated)		0.07%/0.53%
Gain Drift		6 ppm/$^{\circ}C$
Offset Drift		1.7 μV
Offset Error	$4\mu V/14\mu V$	
Maximum Offset Error (Calibrated/Uncalibrated)	$4\mu V/14\mu V$	0.39%/1.67%
Sensitivity	0.02 $^{\circ}C$	

3.9 Instrumentation

A PSSLBG2II2Z venturi model flow meter is used to measure the mass flow at the inlet of the test section. Venturi flow meters use the pressure drop to calculate the mass flow. Pressure drop is created by the increase of the velocity at the throat. After mass flow is measured, an IMV30 series multivariable transmitters are used to transmit the data to the DAQ system. The output signal of the transmitter is between 4 to 20 mA. Also, an RS485 MODBUS module has been used to collect the data from the flow meter. More information is already provided in section 3.8.

A PX1009L0 pressure transducer is used to measure the absolute pressure. Some of the advantages of the pressure transducer are high working temperature, high reliability, and exceptional calibration stability. A pressure transducer converts pressure into an analog electrical signal. After this conversion, a transmitter is used to increase the range to send it over a long distance. The transducer connected to the pipe has a different material to contact the flow based on the technology. However, besides the technology, the actual process is the measuring diaphragm. After deflection sensed by diaphragm, the analog signal is converted to the electrical signal with a pressure transducer. Pressure transducers are located at the inlet and the outlet of the test section to measure pressure drop in the test section.

A PX119 pressure transmitter is used to convert the electrical signal from the transducer. Some of the advantages of the pressure transmitter are its small body size, a single piece of stainless steel with additional protection for internal electronics, and excellent thermal compensated output. The output signal of the transmitter is between 4 to 20 mA. The output range represents 0 to 100% for the sensed physical variable. Thus, the output signal (4 to 20 mA) needs to be calibrated in the operating pressure range, so 4 mA represents the minimum, and 20 mA represents the maximum working pressure.

The unique part of the PHILUS is that the optical fiber sensor is used to measure the temperature. More information is provided in the section 3.1.

Location of the instrumentation is another critical decision in the high-pressure and temperature facilities because with the help of the instrumentation, pressure, temperature, and flow rate can be known in specific locations. Also, it is vital to measure every aspect of the flow condition in the inlet of the test section. Locations of the instrumentation can be seen in Figure 3.15.

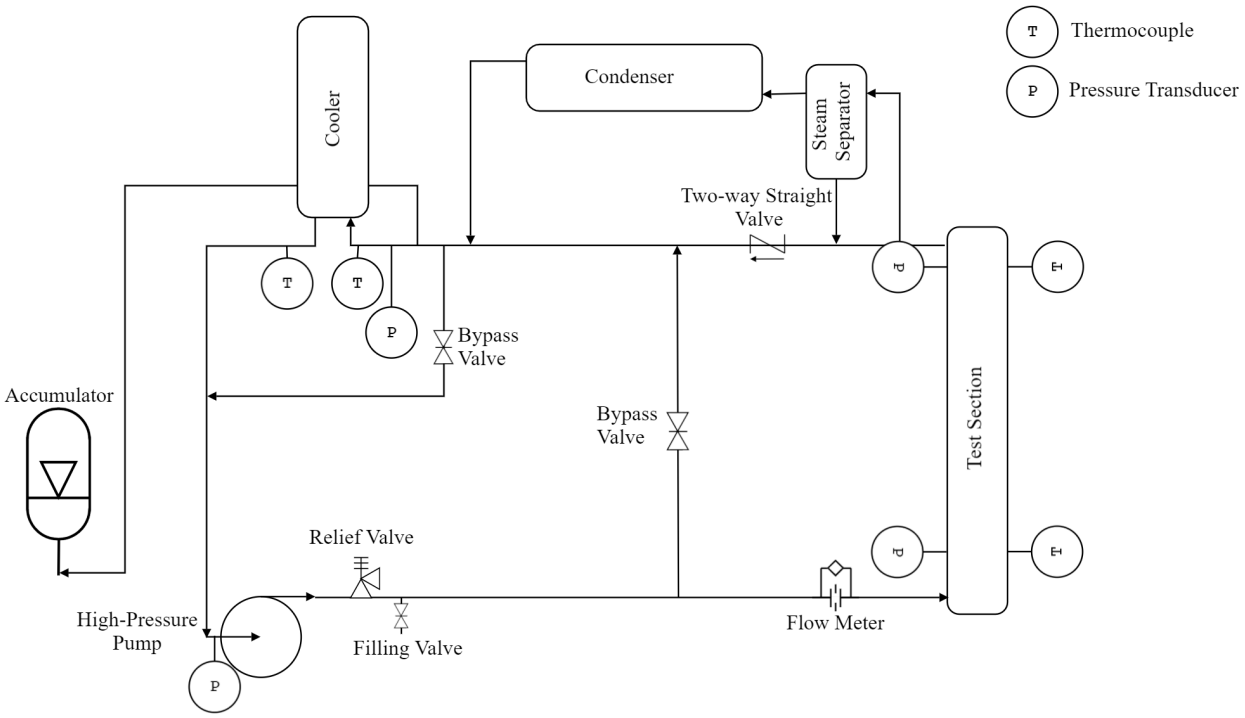

Figure 3.15: Schematic diagram of the PHILUS Facility

Table 3.22: Specification of the instrumentation

Type	Pressure Range (bar)	Accuracy	Working Temperature
PX119 pressure transmitter	Up to 345	0.50%	-40 to 135°C
PX1009L0 pressure transducer	Up to 345	0.25%	-54 to 343°C
Venturi Flow Meter	Up to 620	0.75%	Up to 816°C
IMV30 multivariable transmitters	-	0.075%	-46 to 121°C

3.10 Secondary Loop

The primary purpose of the secondary loop is to maintain coolant for the shell side of both the cooler and the condenser. The secondary loop's main components are secondary piping, a low-pressure pump, two tanks, and control valves.

The secondary side piping is mainly 1.5 inches diameter. This pipe is connected to the shell side of the cooler and the condenser. As shown in Table 3.13, the design temperature of the shell side is 65.55 °C. Also, the design pressure of the shell side is 101 kPa. Thus, the secondary side piping specifications need to be defined based on the shell side limits.

A low-pressure pump maintains the flow in the shell side of heat exchanger components. The pressure drop at this section is significantly lower than the main loop, so the head requirement of the low-pressure pump is much smaller than the high-pressure pump. Calculating the pressure drop is much easier because there is only a single-phase flow. In order to calculate the pressure drop and the friction factor, equations in section 3.5 can be used. There is also another way to calculate the friction factor. After calculating relative pipe roughness (k) and the Reynolds number (Re) with Eq. 3.38 and 3.14, respectively.

$$k = \frac{\epsilon}{d} \tag{3.38}$$

The Moody diagram, which is in Table 3.16 can be used to find the Darcy–Weisbach friction

Table 3.23: Specification of low-pressure pump

	Item	Value
Requested	Flow rate (GPM)	20
	Differential head (ft)	30
	Working Pressure (atm)	1
	Working temperature ($°C$)	Up to 80
Designed	Maximum working temperature ($°C$)	110
	Maximum head (ft)	31.5
	Maximum working pressure (psi.g)	13.63

factor.

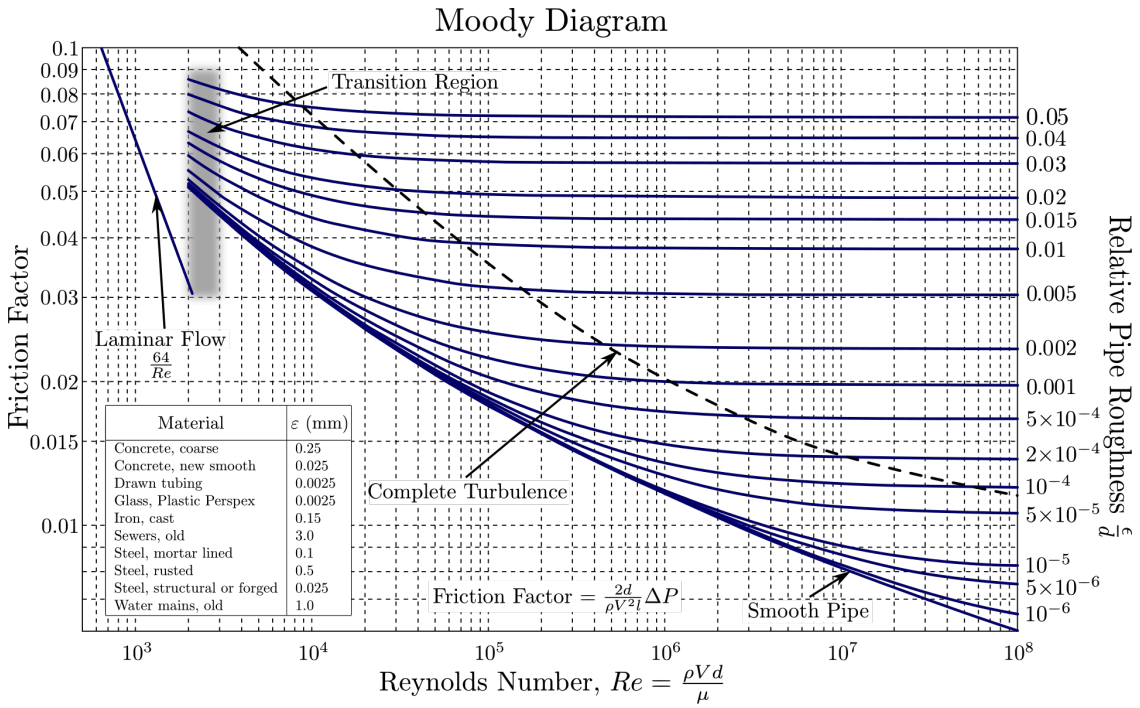

Figure 3.16: Moody diagram for the friction factor [29]

After finding the friction factor, Eq. 3.22 can be used to calculate the frictional pressure drop. Eq. 3.29 can be used to calculate the pressure drop due to gravity. With this calculation, a Wilo Stratos-MAXO 1.25x3-30 has been used for the low-pressure pump. Specification of the low-pressure pump is in Table 3.23.

Another component of the secondary loop is two 268-Gallon tanks. Even though the volume of the loop is around 10 liters, the tank volume used for coolant is around 2029 liters. The reason for this considerable difference is thermal inertia. With the help of thermal inertia, it is easier to control the temperature in the secondary loop. Also, initial analysis showed the need to install a chiller for the tanks to run the loop for longer time. Without a cooling system the secondary side tanks, the loop can only run around 3 hours which is not enough to obtain CHF.

The last main component of the secondary loop is the control valve. The control valve is used to regulate the flow in the shell side of both heat exchange components. With this regulation, the heat transfer rate can be controlled.

3.11 Support structure

The support structure of the loop is designed for higher strength because of safety considerations. Front and side views of the support structure can be seen in Figure 3.17, and the specification of frames in the support structure is in Table 3.24. Bolts have been used to connect frames, which is shown in Figure 3.18.

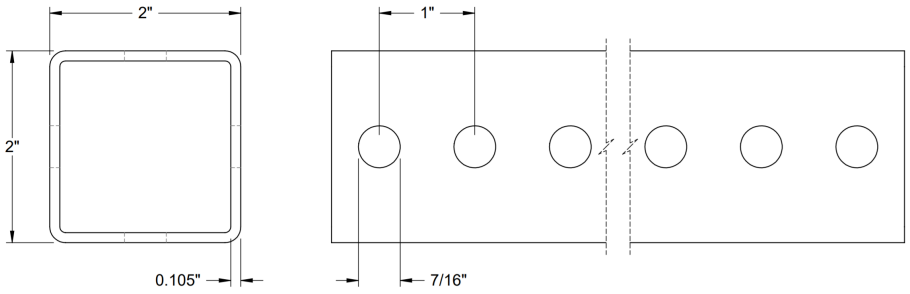

Figure 3.17: Front and side views of the support structure

Table 3.24: Specification of tubes in the support structure

Framing Type	**Bolt together**
Material	Steel
Height × Width	2 × 2 (in)
Wall thickness (in)	0.105
Yield Strength (psi)	60000

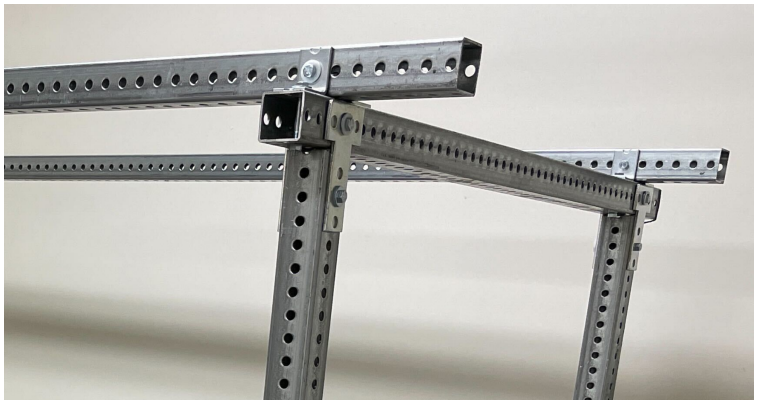

Figure 3.18: Bolting the support structure

Springs and pivoting threaded loop hangers are used to stabilize the pipes horizontally. However, these components are not suitable for vertical usage, so the main bypass and the test section are immobilized with the help of springs that are shown in Figure 3.19.

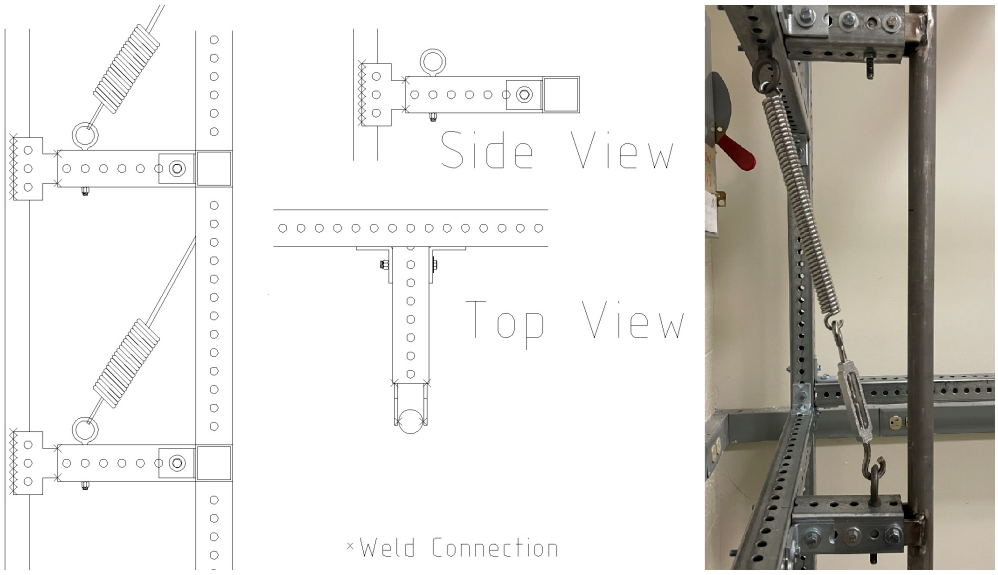

Figure 3.19: (Left) The Schematic of the Test Section Connection (Right) Picture of the Test Section Connection

The last version of the PHILUS facility is shown in Figure 3.20. The support structure is bolted to the floor.

The PHILUS facility can investigate CHF and post-CHF under 18 MPa between 500 and 3700 kg/m^2s at 357°C. The test section of the PHILUS facility is designed to mimic the PWR core flow area to power ratio and rod diameter. Also, the working pressure, mass flux, and temperature can be set to work under PWRs conditions. With these inputs, the Reynolds number of the PHILUS facility can be the same as PWRs. With the help of the optical fiber temperature sensors, the surface temperature at the CHF and post-CHF can be investigated with a very high spatial resolution of less than one millimeter over the 1-meter heated length. Components are designed to have desired inlet and outlet conditions at the test section. During the design, flexibility was one of the main focuses for future upgrades.

Figure 3.20: The PHILUS Facility

Chapter 4

COBRA-TF (CTF) Simulation

During this chapter, Coolant-Boiling in Rod Arrays–Two Fluids (COBRA-TF) will be briefly explained. Groeneveld's look up table [30] for CHF predictions was used to design an initial experimental matrix. The expected CHF, void fraction, and flow regime are shown in this Chapter. Also, Barnett's data was simulated in CTF to understand errors between simulations and experimental results. The purpose of this chapter is to provide guidance for experiments.

4.1 COBRA-TF

COBRA-TF is a computational tool for subchannel analysis. Pacific Northwest National Laboratory (PNNL) developed it in 1980. It was initially a thermal-hydraulic rod-bundle analysis code, but it is kept updated over time. The code uses a two-fluid modeling approach with three separate flow fields (fluid flow, vapor, and liquid droplets). COBRA-TF includes a wide range of T/H (thermal-hydraulic) models crucial to accurate LWR safety analysis, including, but not limited to, flow regime dependent two-phase heat transfer, inter-phase heat transfer and drag, droplet breakup, and quench-front tracking [31].

CTF is an updated version of COBRA-TF by the Pennsylvania State University (PSU), and the North Carolina State University did the last update of the CTF. It is a 1-D transient code that solves each flow field's energy, mass, and axial and transverse momentum equations.

Rods and subchannels need to be defined in the code, and all of the subchannels can be simulated separately. In the PHILUS test section, there is one rod and four subchannels, as shown in Figure 4.1. Even though the test section is axis-symmetric, this symmetry was not used during the CTF simulation because the average value of the four subchannels was used.

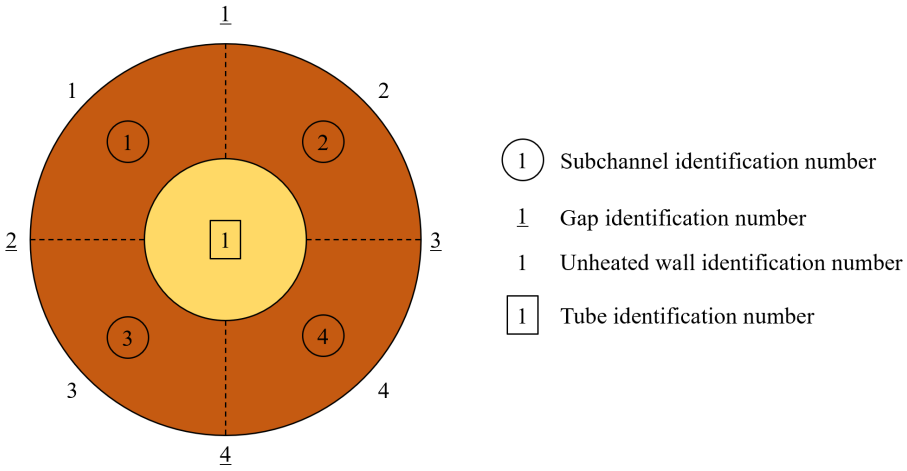

Figure 4.1: CTF subchannels

The boundary conditions for every subchannel need to be carefully defined after the subchannel's geometry, rod's geometry, and material properties are well defined. The last step is to define the model. The model choices used for the PHILUS's simulation are shown in Table 4.1, based on the recommended values.

Table 4.1: CTF main model choices

Parameter	**Model Chosen**	**Card**	**Option**
Rod friction	$\lambda = 0.204Re^{-0.2}$	1.1	2
Mixing and void drift model	Neither mixing nor void drift	1.1	0
Fluid property tables	Original CTF water property tables	1.1	0
Conduction model flag	Radial conduction only	8.1	1
Number of radiation channels	No radiation is modeled	8.1	0
Critical heat flux (CHF)	No correlation	8.1	-1
Choice for nucleate boiling model	Thom's choice	8.1	1
DNB check option	Groeneveld look-up table	8.1	3

The numerical convergence of Thom's correlation is faster than Chen's correlation. Also, neither mixing nor void drift models were chosen because of the symmetry in the test section. In table 4.1, Groeneveld look up table is used to check whether or not DNB was achieved. Because the CHF option is not selected, the code will not simulate the post-CHF regime

4.2 COBRA-TF on the PHILUS

Outlet pressure, inlet mass flux, and inlet subcooling of the test section are the three defined boundary conditions during the simulations. Outlet pressure of the test section boundary condition was set to 7, 9, 11, 13, 15, and 17 MPa. The inlet subcooling range is 100 kJ/kg to 400 kJ/kg. Inlet mass flux boundary conditions are from 500 kg/m^2s to 3500 kg/m^2s and it

increases by 500 kg/m^2s for each pressure and subcooling simulation. With these boundary conditions, there are 168 different test section simulations. Example of the CTF code is shown in Appendix B, and some information of the simulations are shown in Appendix C. During the simulations, CHF is observed by increasing the power by one kW/s. Departure from nucleate boiling ratio (DNBR) output was used to determine if the simulation reaches the CHF. As mentioned before, the DNB check option chosen Groeneveld look-up table shown in Table 4.1 and the reason behind this choice is explained in section 4.2.1. If the DNB ratio is lower than one, it means that the current local heat flux is higher than the necessary heat flux to reach CHF, as shown in Figure 4.2. Since the power increases 1 kw per second, the CHF prediction of Groeneveld's is decreasing while local heat flux in the rod increases. After a certain time, the local power is slightly higher than the prediction, so it means that the CHF occurs at that location. Since the power is linear in the test section, it is expected to reach CHF near the outlet of the test section.

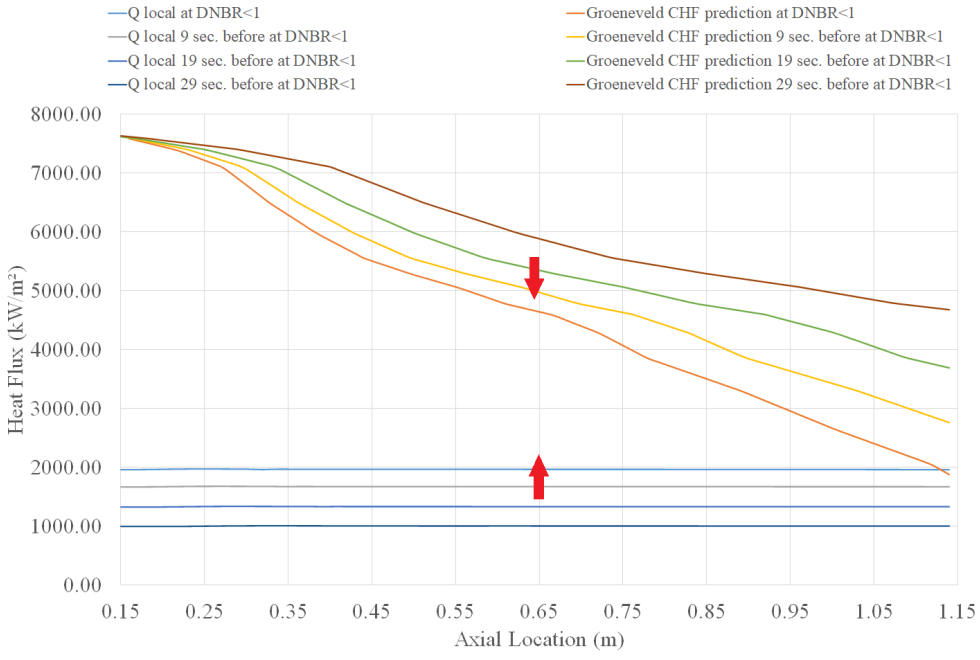

Figure 4.2: Iterative Procedure to Determine the Predicted CHF Value and Associated Properties

The number of vertical levels is 132 equal pieces, and each mesh has a 0.01 m length as shown in Figure 4.3. Thus, the heated section in the simulation is from the 14th node to the 114th node. All the results shown in the following chapter are when CHF occurs at the last four nodes.

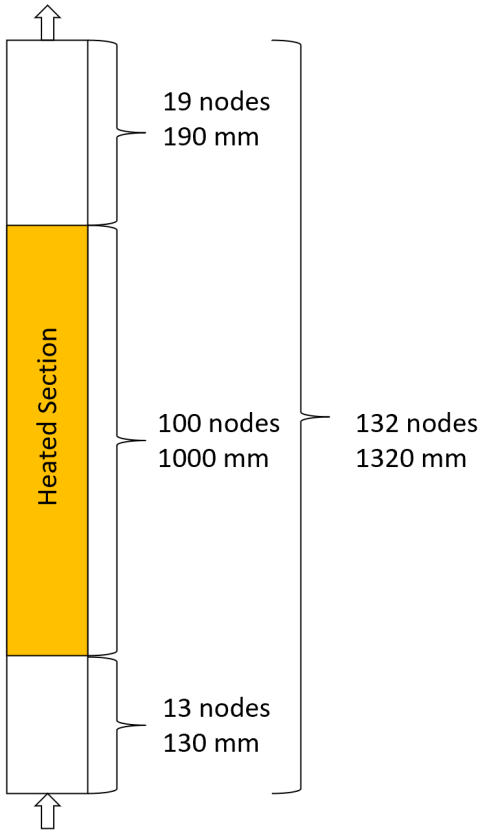

Figure 4.3: Axial schematic of the PHILUS Facility Test Section

4.2.1 Comparison of the DNB check options

In the DNB check options, the Groeneveld look-up table is the most suited option for the working condition of the PHILUS facility. Forty-eight (48) simulations are performed to compare the results of different options at the maximum and minimum pressures and mass fluxes in the four different subcooling conditions. The three options are Groeneveld's look-

up table, W(Westinghouse)-3 correlation, and the Biasi model. Working conditions for each correlation are shown in Table 4.2.

Table 4.2: Range of Operating Conditions of DNB check option

DNB Check Option	**Parameters**	**Min**	**Max**
W(Westinghouse)-3	Pressure (MPa)	5.515806	15.85794
	Mass Flux (kg/m^2s)	1356.231	6781.154
	D_{heated} (m)	0.003	0.0375
	Local steam quality	-0.15	0.15
	Length (m)	0.245	3.6576
Biasi	Pressure (MPa)	0.27	14
	Mass Flux (kg/m^2s)	100	6000
	D_{heated} (m)	0.003	0.0375
	Local steam quality	$f(\rho_l, \rho_g)$	1
	Length (m)	0.2	6
Groeneveld	Pressure (MPa)	0.1	21
	Mass Flux (kg/m^2s)	0	8000
	D_{heated} (m)	0.025	0.003
	Local steam quality	0.9	-0.5

The maximum applicable pressure of W-3 correlation is lower, and the minimum mass flux is higher than the PHILUS's working conditions. Also, the local steam quality range is not enough for the high-quality CHF. On the other hand, Biasi has the same limit in pressure and is suitable of subcooled conditions.

Table 4.3 shows the local heat when CHF occurs for all DNB check options.

Table 4.3: Local Heat Flux of W-3, Biasi, and Groeneveld at CHF

			DNB check option						
			Groeneveld Look-up Table	W-3	Biasi				
Pressure (MPa)	Mass Flux (kg/m²s)	Inlet Subcooling (kj/kg)	Local Heat Flux (kW/m²)			-20% of LUT	20% of LUT	W-3Error (%)	Biasi Error (%)
7	500	100	1975.09	1975.06	2240.61	1580.07	2370.108	0.00	-13.44
		200	2109.11	2142.62	2373.00	1687.29	2530.932	-1.59	-12.51
		300	2209.80	2276.66	2542.20	1767.84	2651.76	-3.03	-15.04
		400	2304.97	2444.21	2675.06	1843.98	2765.964	-6.04	-16.06
17		100	802.49	1874.89	1297.94	641.99	962.988	-133.63	-61.74
		200	903.03	2478.04	2142.62	722.42	1083.636	-174.41	-137.27
		300	1003.57	3148.19	2276.66	802.86	1204.284	-213.70	-126.86
		400	1104.10	-	2444.21	883.28	1324.92	-	-121.38
7	3500	100	-	-	-	-	-	-	-
		200	-	-	-	-	-	-	-
		300	-	-	-	-	-	-	-
		400	-	-	-	-	-	-	-
17		100	2243.47	1874.89	3248.63	1794.78	2692.164	16.43	-44.80
		200	2712.58	2478.04	-	2170.06	3255.096	8.65	-
		300	3181.69	3148.19	-	2545.35	3818.028	1.05	-
		400	-	-	-	-	-	-	-

Empty cell (-) shows that the power was not enough to reach CHF at defined conditions. At 500 kg/m^2s mass flux and 17 MPa, W-3 simulations prove that the correlation cannot predict the CHF. Also, it is only suited to low-quality applications. On the other hand, the Biasi simulations show that the model is not suited for the 17 MPa applications. Thus, Groeneveld's look-up table is the most suited DNB check option for the PHILUS facility.

4.2.2 CHF Power

During the 168 simulations, one of the first parameters to look for is the power of the test section required to reach CHF. Figure 4.4 and Figure 4.5 show the necessary power at the test section to reach CHF with different inlet and outlet conditions.

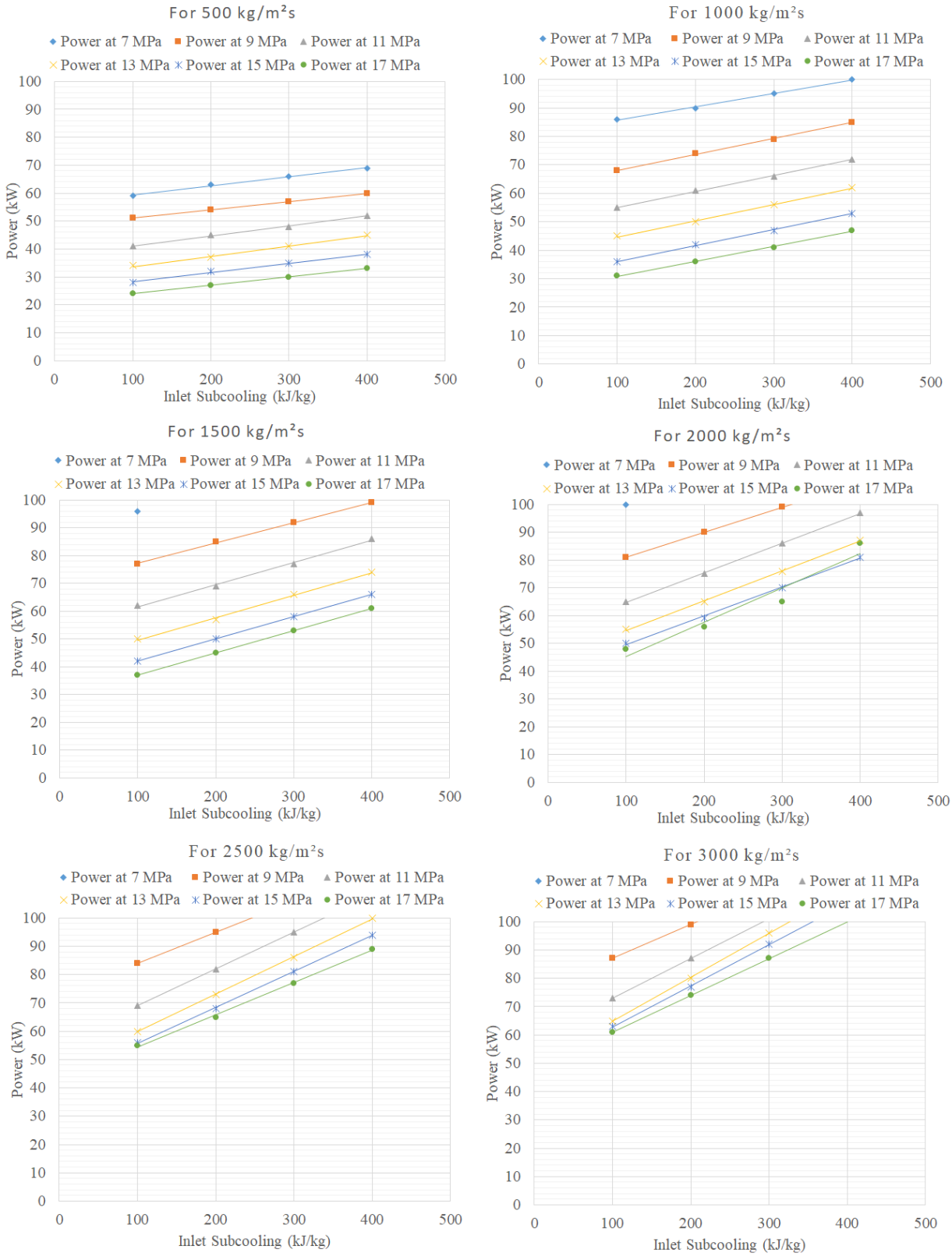

Figure 4.4: Test section power at CHF at 500-3000 $^{kg}/_{m^2s}$

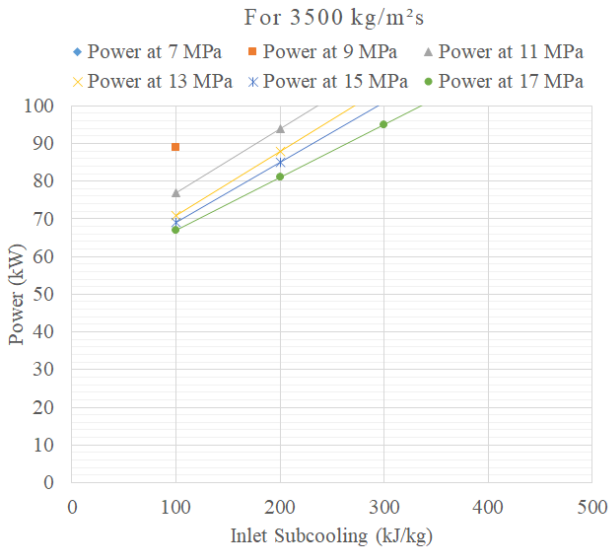

Figure 4.5: Test section power at CHF at 3500 $^{kg}/_{m^2 s}$

In the lowest mass flux, all simulations reach the CHF while it needs more power at the higher mass flux. Even though the necessary power is much higher in the higher mass fluxes, the PHILUS's test section can reach CHF at higher pressure.

4.2.3 Necessary Heat Flux at CHF

The designed maximum heat flux of the test section is 3350 $^{kW}/_{m^2}$. The necessary heat flux to reach CHF is shown in Figure 4.6 and Figure 4.7 for several conditions.

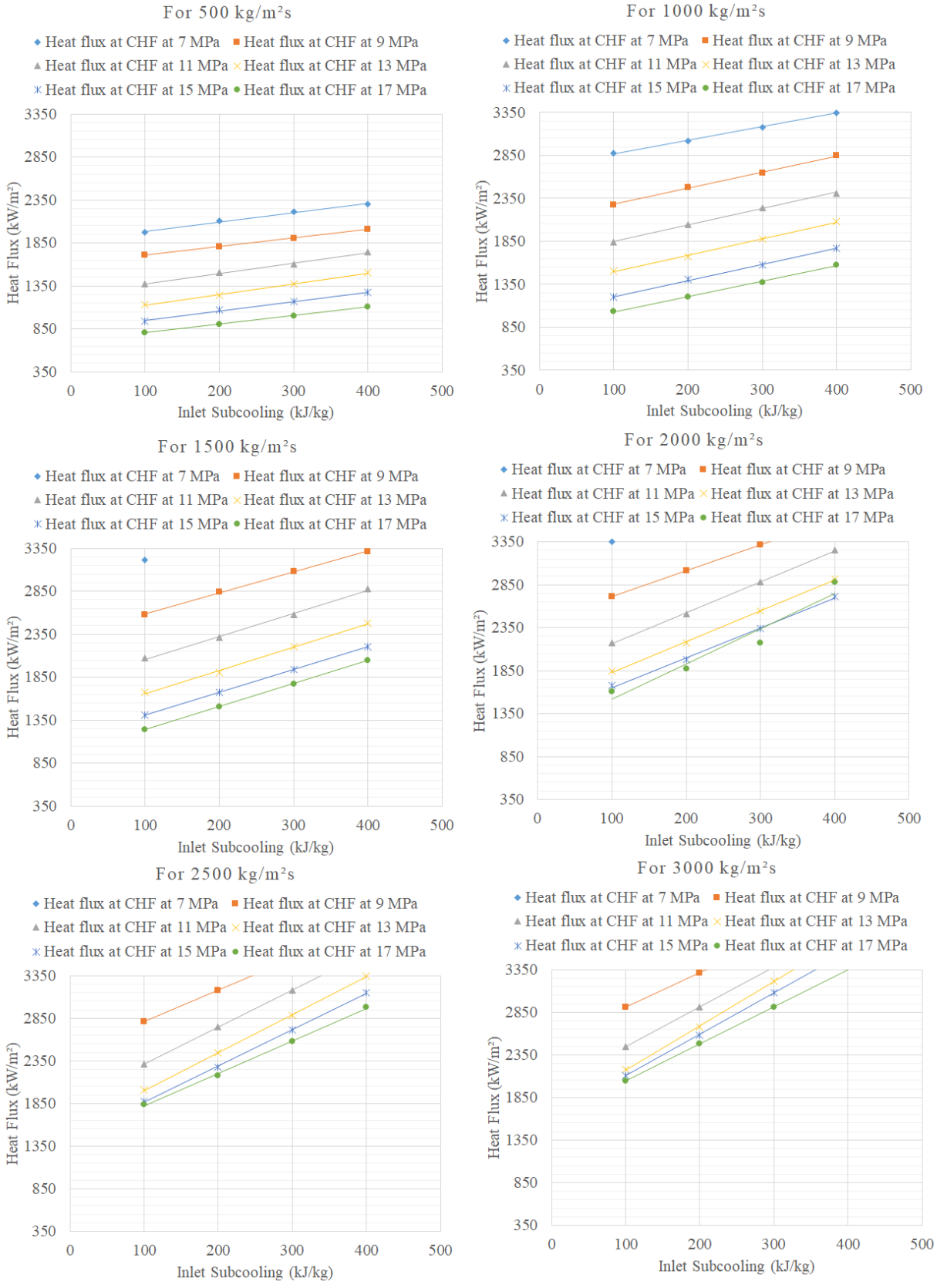

Figure 4.6: CHF at 500-3000 $^{kg}/_{m^2s}$

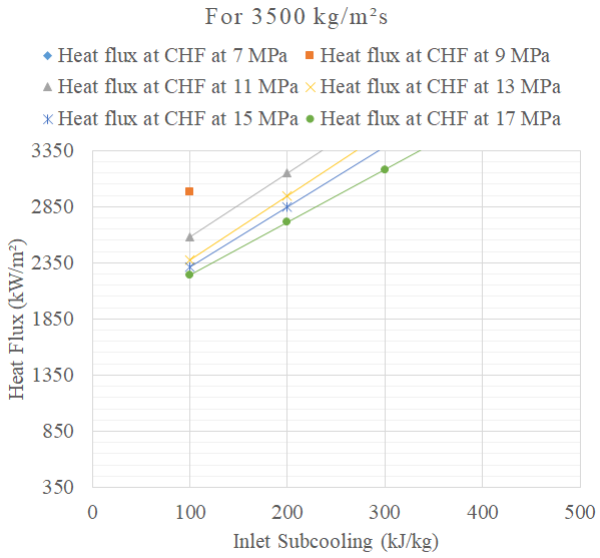

Figure 4.7: CHF at 3500 $^{kg}/_{m^2s}$

As mentioned in 2.1.3, CHF increases with the increase of the mass flux and inlet subcooling while it decreases with the increase of the pressure after 5-6 MPa. Even though the maximum heat flux ($3350 kW/m^2$)is the limit of the PHILUS facility, the facility can reach CHF in 129 out of 168 simulations.

4.2.4 Direct Comparison with Groeneveld Look Up Table

The Groeneveld's look-up table is derived in a particular case with the upward flow in an 8-mm uniformly heated tube. However, it can be used in different geometries and flow conditions. To use the table for different cases, the correction factor needs to be multiplied with the look-up table's CHF value [30]. In the beginning, Groeneveld suggests that heated diameter is the correction factor, yet the authors suggest that hydraulic diameter equivalent is more appropriate [32]. With this change, the correction factor is defined by Eq. 4.1.

$$K_1 = \max\left(0.57, \sqrt{\frac{8\text{mm}}{D_{hy}}}\right) \tag{4.1}$$

where D_{hy} is the hydraulic diameter as in Eq. 4.2

$$D_{hy} = 4\frac{A}{P_w} \tag{4.2}$$

where P_w and A are wetted perimeter and flow area, respectively.

The correction factor is 1.302 ($K_1 = 1.302$) in the test section of the PHILUS.

The results of the CTF simulation and the Groeneveld prediction (hand-calculation) are compared to show that the results of the CTF are accurate. Figures 4.8 shows a comparison of the CTF and Groeneveld prediction.

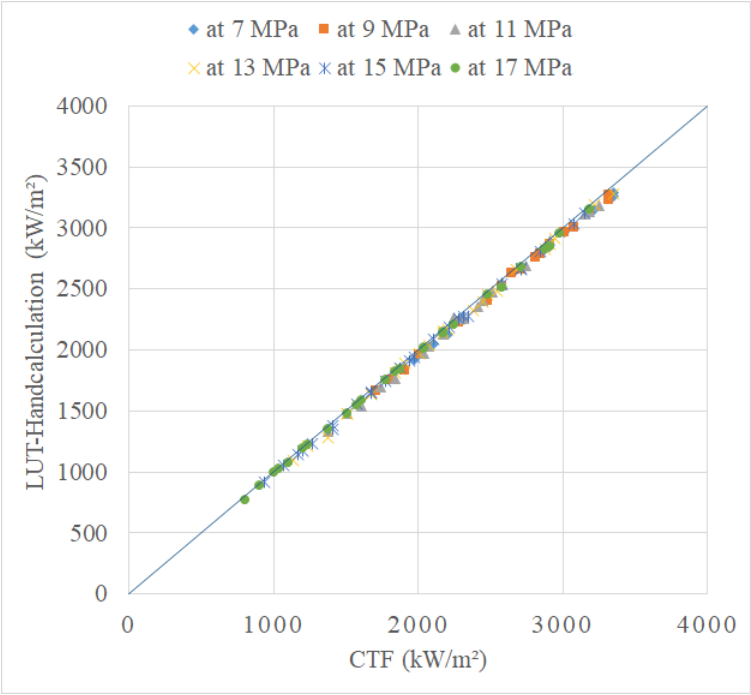

Figure 4.8: Comparison of CTF Local Heat Flux and Look-Up Table Hand calculation

The percentage differences between the CTF results and the Groeneveld look-up table is less than five percent. CHF calculates the local pressure and as shown in the next section, the void fraction and equivalent flow regime.

4.2.5 Void Fraction

The void fraction is used to determine the flow regime in CTF. The flow regime selection logic is shown in Figure 4.9. Figure 4.10 shows the illustration of the flow regimes. When the maximum wall surface temperature in mesh cell is lower than critical heat flux temperature, the normal flow regime map is used to determine the flow regime. Equation 4.3 is used to determine the critical heat flux temperature [31].

$$T_w = min(705.3^\circ F, T_{CHF}) \tag{4.3}$$

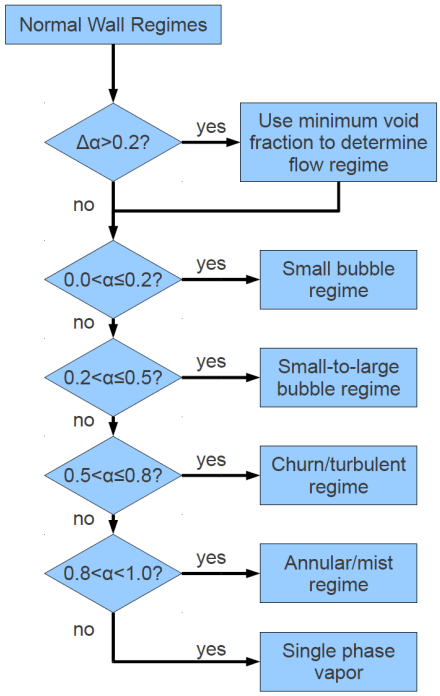

Figure 4.9: Flow Regime Selection Logic [31]

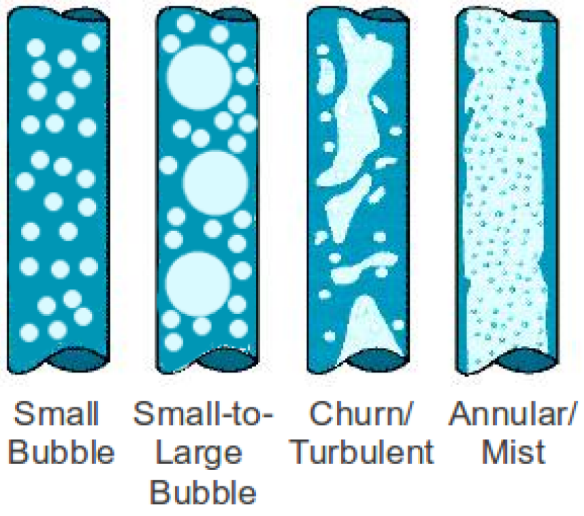

Figure 4.10: Flow Regime Recognized by CTF [31]

Small bubbles are dispersed in the flow in the small bubble regime for $0.0 < \alpha \leq 0.2$. When the void fraction is between 0.2 and 0.5 ($0.2 < \alpha \leq 0.5$), small bubbles start to attach,

and this regime is known as the slug regime (small-to-large bubble). Churn/Turbulent flow regime occurs when void fraction is between 0.5 and 0.8 ($0.5 < \alpha \leq 0.8$). This regime occurs after the slug regime until a stable film forms, and the annular regime starts. All of the boundary conditions for each regime are determined by various research data [31].

Figure 4.11 and Figure 4.12 show the void fraction and the flow regime for simulations.

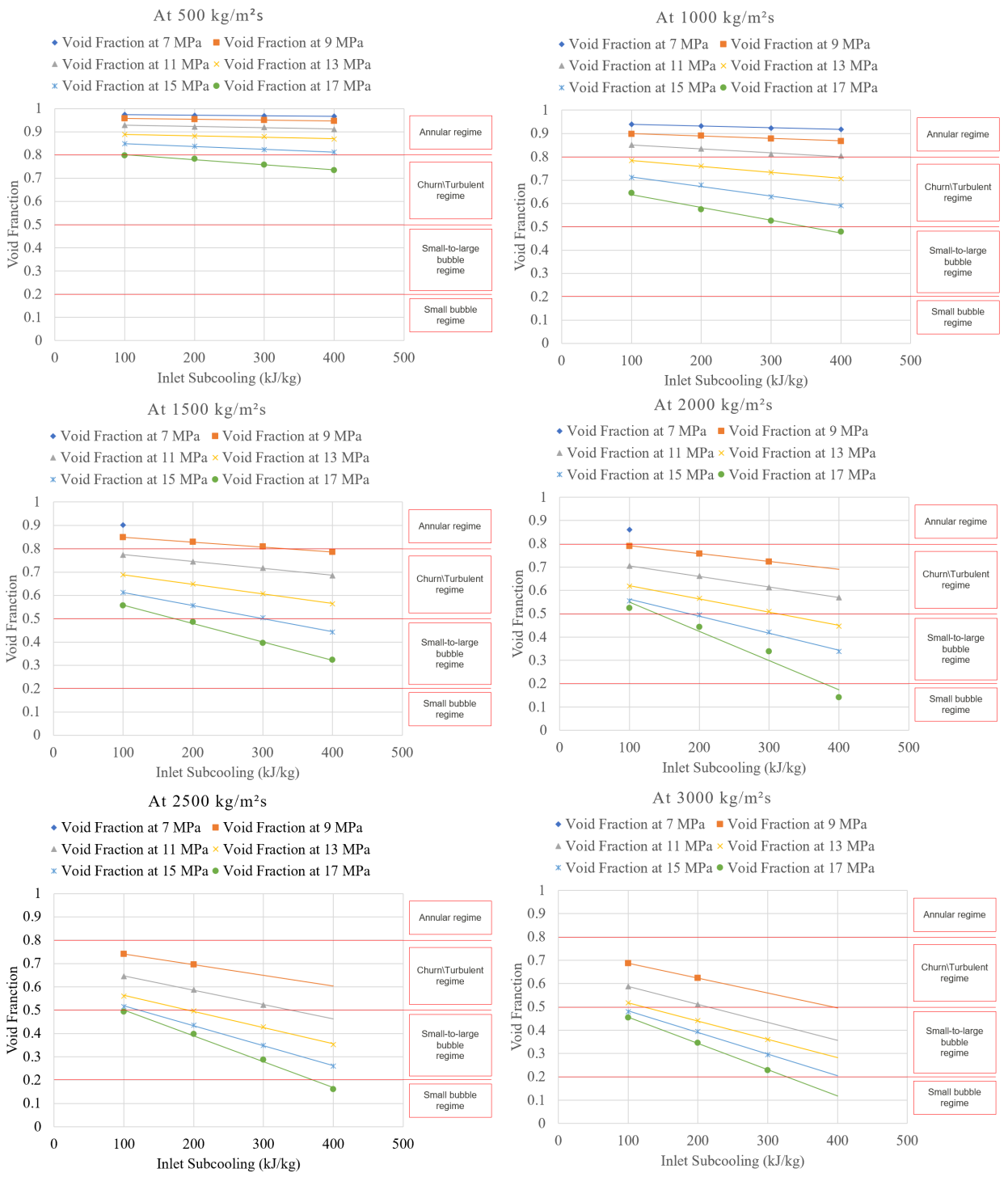

Figure 4.11: Void Fraction and Flow Regime at 500-3000 $^{kg}/_{m^2s}$

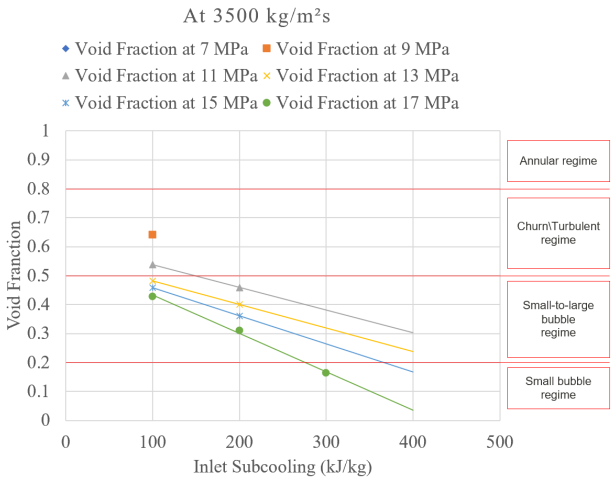

Figure 4.12: Void Fraction and Flow Regime at 3500 $^{kg}/_{m^2s}$

At low pressure, the void fraction is higher than 0.8, and the flow is in an annular regime. The void fraction decreases with an increase in the mass flux, pressure, and inlet subcooling. These simulations show that the PHILUS facility will have all of the flow regimes.

4.2.6 Pressure Drop in the Test Section

The last subject to investigate in CTF is the pressure drop in the test section. Since the outlet pressure of the test section is the boundary condition, pressure drop needs to be carefully defined to have an accurate pressure at the inlet of the test section. Pressure drop is measured by the difference between the inlet and the outlet pressure output in CTF. Figure 4.13 and Figure 4.14 show the pressure drop in the heated test section. Pressure drop increases with the increase of the mass flux, yet it decreases with an increase in pressure and subcooling. The maximum pressure drop occurs at 7 MPa at 100 $^{kj}/_{kg}$ at 2000 $^{kg}/_{m^2s}$ with 176.67 kPa because this is the last condition that the test section reaches the CHF at minimum tested pressure.

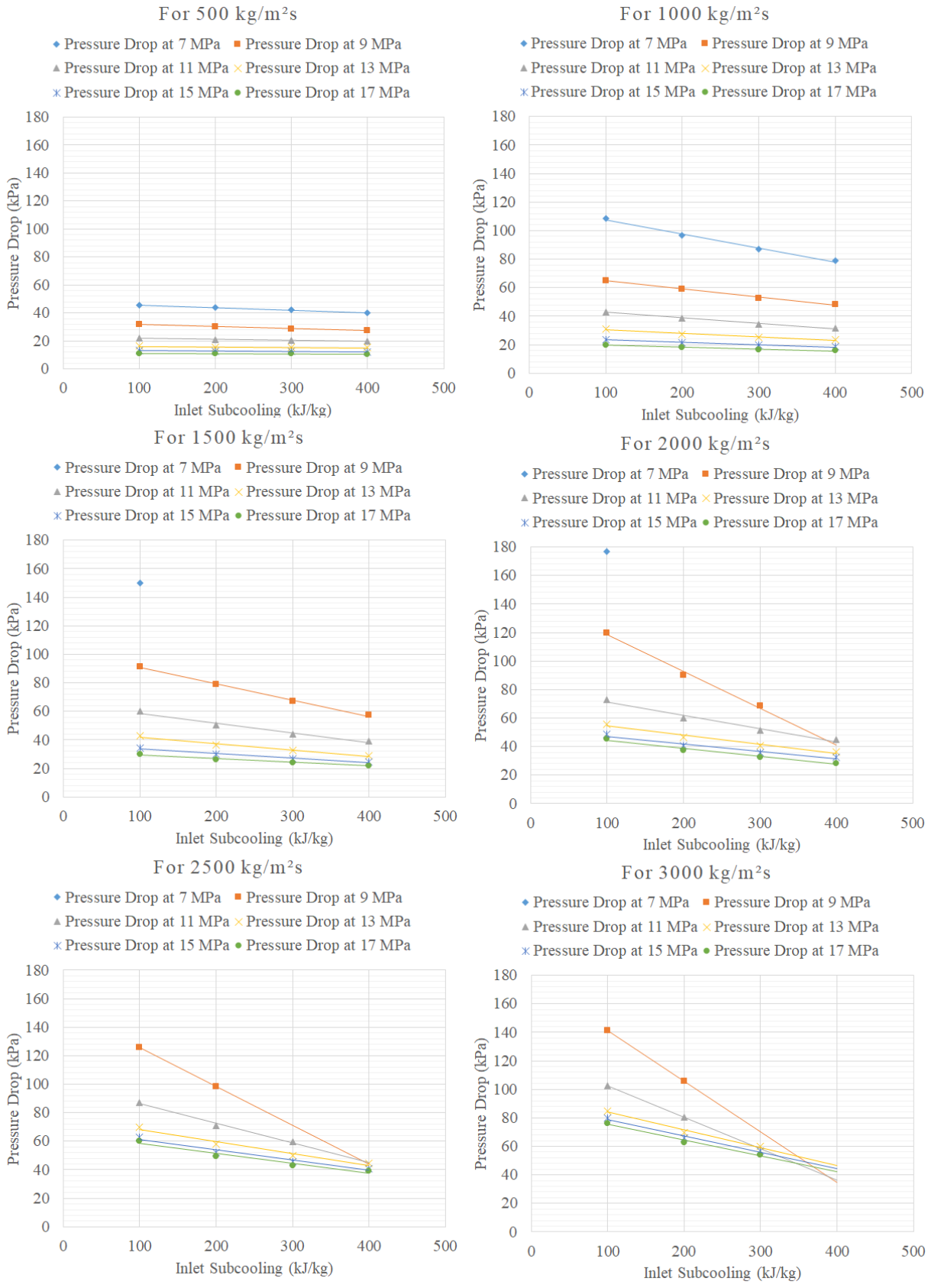

Figure 4.13: Pressure Drop at 500-3000 $^{kg}/_{m^2s}$

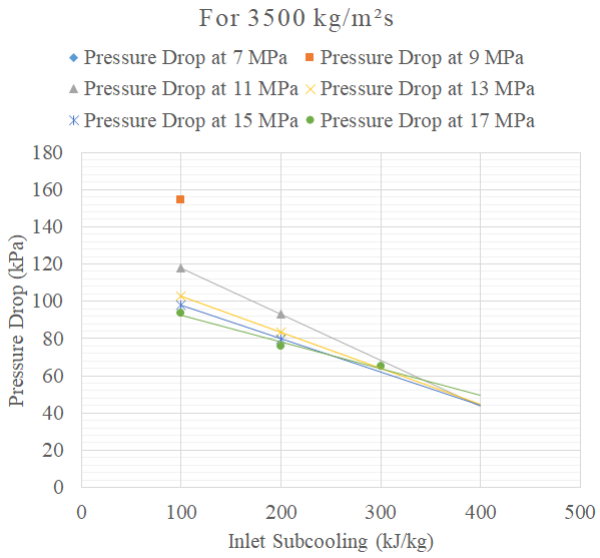

Figure 4.14: Pressure Drop at 3500 $^{kg}/_{m^2s}$

Pressure drop results show that the high-pressure pump can work under the PHILUS's working conditions while the test section is heated. With the help of simulation and the CTF simulation, it can be seen that the high-pressure pump is suitable to the PHILUS's working conditions.

4.3 Simulation of Barnett's data

In this section, Barnett's experimental data and its CTF simulation are compared [33]. Since there is no experimental data for the PHILUS facility at this point, these simulations give a rough idea about the expected error. Figure 4.15 shows the comparison of the first fifty experimental data of the compilation of 1000 p.s.i.a annulus burnout data and its CTF simulation. In Barnett's data, there were 2 different hydraulic diameters. Mass flux is from 750 to 3100 kg/m^2s, and the inlet subcooling is between 60 and 935 kJ/kg at 1000 p.s.i.a.

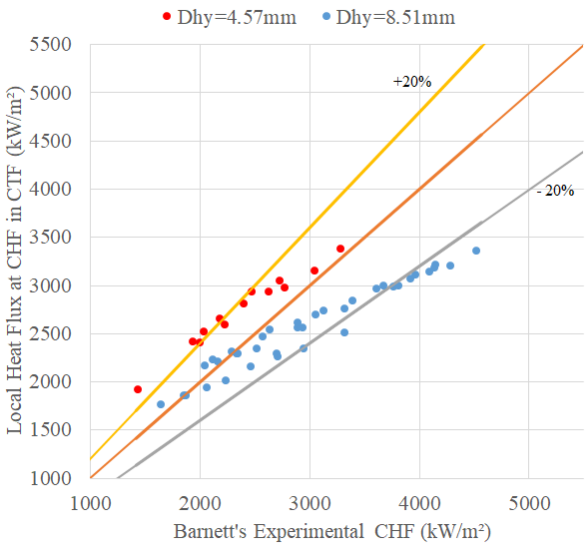

Figure 4.15: Comparison of Barnett's data and its CTF simulation

It is seen in Figure 4.15, the error between the experimental CHF and simulation in CTF can be more than 20%, so even though not all the parameters are the same with the PHILUS facility, 20% error can be expected.

In this chapter, the capability of the PHILUS facility is shown with CTF simulations. The PHILUS facility is capable of investigating CHF under various conditions. Also, Barnett's data simulations show that the CHF is a very complex phenomenon, and current predictions need more data to reduce the error.

Chapter 5

Conclusions and Future Work

The high-Pressure HIgh-temperature annuLUS flow (PHILUS) Facility was designed as part of this thesis. The test section was designed and manufactured to mimic a PWR core subchannel. The design power of the test section is 100 kW, and it is operable at up to 22 MPa at 370°C. The test section is designed to incorporate optical fiber temperature sensors to measure heat transfer during transients. TRACE and CTF computational codes were used to design the facility and develop an initial experimental matrix. Additionally, Barnett's data in an annular flow channel were simulated using CTF since their experimental conditions are comparable to the PHILUS.

In the primary loop, all components of the PHILUS facility were carefully investigated to ensure that the working conditions of the facility could be reached. First, the heat exchangers were designed to have enough capability to cool single-phase and two-phase flow. After that, the steam separator was designed to direct vapor to the condenser and to provide stability to the test section. A bladder-type accumulator was chosen to cope with the pressure oscillation and thermal expansion. The volume of the accumulator was carefully calculated. The high-pressure pump head was determined using TRACE's pressure drop prediction. A custom-design Teikoku pump was selected for the facility. A bypass line was designed to minimize the pump-head requirements and to have the most suited control of the flow rate in the test section inlet. The facility will be instrumented with thermocouples, optical fibers, and pressure transducers connected to the data acquisition (DAQ) system, which will

be connected to LabView to control its operation. The last step was to connect all the equipment with piping. 3/4 inches schedule 160 stainless steel 316/L (Sch 160 SS 316/L) pipes are used in the loop except between the outlet of the cooler and the inlet of the pump. Between these two components, 1-inch pipes were used to minimize the suction side's resistance, reduce the friction loss, and increase the NPSH. Socket welded flanges were used to disassemble and assemble most of the components. Steel bolt-together frames were used to build the support structure for the primary and the secondary loop.

The secondary loop consists of two tanks, a VFD-controlled low-pressure pump, valves, and piping. The main purpose of the secondary side is to provide coolant to the heat exchangers. One of the other purposes is to cool the rod extremities and pump motor.

Furthermore, CTF was used to investigate the PHILUS facility's capability. CTF results reveal that the facility can reach CHF under various conditions and flow regimes. During CTF simulation, W-3 correlation, Biasi model, and Groeneveld look-up table were used as DNB check options, and the Groeneveld look-up table is the most suited DNB check option for the PHILUS facility's working conditions.

Also, this study shows that the PHILUS facility has unique features, such as the optical fiber sensor and the working conditions. Because of the high-pressure and high-temperature working conditions, all the main components were specifically manufactured for us by private companies. The supply chain was affected by COVID-19, and it extended the lead-time of major components. Therefore, the facility is still under construction. The transformer, chiller for the tanks on the secondary side, and exact details of some of the instrumentation were out of the scope of this study. Undefined components situation is shown in table 5.1.

Also, a test plan needs to be developed. The test helps to monitor if all of the equipment works properly. After the test plan, the start-up and shut-down procedure needs to be

Table 5.1: Undefined Components Situations

Component	**Status**
Thermocouples	Ready to Order
Chiller	Ready to Order
Transformer	In Progress
Accumulator Cooler	In Progress
Secondary Pipe	In Progress
Bypass Valves	In Progress

carefully designed to run the experiments without damaging the components. The PHILUS facility can be updated because flexibility was one of the most critical parameters during the design. A preheater and a precooler can be attached before the test section's inlet to the better control inlet temperature. The CTF simulations and the PHILUS facility designed during this work will be used by future graduate students and researchers to investigate and improve our current post-CHF heat transfer models.

Reference

1. Nukiyama, S. The maximum and minimum values of the heat Q transmitted from metal to boiling water under atmospheric pressure. *International Journal of Heat and Mass Transfer* **9,** 1419–1433 (1966).

2. Iea. *World total final consumption by source, 1971-2019 –nbsp;charts – Data amp; Statistics* https://www.iea.org/data-and-statistics/charts/world-total-final-consumption-by-source-1971-2019-accessed-on-3/11/2022.

3. Liu, Q., Shi, S., Sun, X. & Kelly, J. Thermal hydraulic performance analysis of a post-CHF heat transfer test facility. *Nuclear Engineering and Design* **339,** 53–64 (2018).

4. Moon, S.-K., Chun, S.-Y., Cho, S., Kim, S. & Baek, W. An experimental study on post-chf heat transfer for low flow of water in a 3x3 rod bundle. *Nuclear Engineering and Technology* **37** (2005).

5. Anghel, I. G., Anglart, H. & Hedberg, S. *Study of post dryout heat transfer in annulus with flow obstacles* in *International Heat Transfer Conference* **49378** (2010), 917–925.

6. Bucci, M., Seong, J. H., Buongiorno, J., Richenderfer, A. & Kossolapov, A. *IR-thermography-based investigation of critical heat flux in subcooled flow boiling of water at atmospheric and high pressure conditions* tech. rep. (Oak Ridge National Lab.(ORNL), Oak Ridge, TN (United States), 2017).

7. Statham, B. & Novog, D. The effects of transient conditions on the onset of intermittent dryout during blowdown. *Nuclear Engineering and Design* **317,** 118–132 (2017).

8. Duarte, J. P., Zhao, D., Jo, H. & Corradini, M. L. Critical heat flux experiments and a post-CHF heat transfer analysis using 2D inverse heat transfer. *Nuclear Engineering and Design* **337,** 17–26 (2018).

9. Avery, M. *et al.* Critical heat flux in TRIGA-fueled reactors cooled by natural convection. *Nuclear science and engineering* **172,** 249–258 (2012).

10. Zhang, R., Duarte, J. P., Cong, T. & Corradini, M. L. Investigation on the critical heat flux in a 2 by 2 fuel assembly under low flow rate and high pressure with a CFD methodology. *Annals of Nuclear Energy* **124,** 69–79 (2019).

11. Duarte, J. P. *Understanding the Minimum Film Boiling Temperature in Two-Phase Flow* (The University of Wisconsin-Madison, 2018).

12. Bestion, D. *et al.* Review of TRACE V5. 0. *US NRC Adams Accession Nos. ML082540133, ML090770758, ML090770759, ML090770760, ML090770761, and ML080810003, US Nuclear Regulatory Commission* (2008).

13. Todreas, N. E. & Kazimi, M. S. *Nuclear systems volume I: Thermal hydraulic fundamentals* (CRC press, 2021).

14. Berenson, P. J. Film-boiling heat transfer from a horizontal surface (1961).

15. Henry, R. Correlation for the minimum wall superheat in film boiling. *Trans. Amer. Nucl. Soc* **15,** 420–421 (1972).

16. Groeneveld, D. & Stewart, J. *The minimum film boiling temperature for water during film boiling collapse* in *International Heat Transfer Conference Digital Library* (1982).

17. Chun, S.-Y., Chung, H.-J., Hong, S.-D., Yang, S.-K. & Chung, M.-K. Critical heat flux in uniformly heated vertical annulus under a wide range of pressures 0.57 to 15.0 MPa. *Nuclear Engineering and Technology* **32,** 128–141 (2000).

18. Anghel, I. G. *Experimental Study of Post-Dryout Heat Transfer in Annuli with Flow Obstacles* PhD thesis (KTH Royal Institute of Technology, 2011).

19. Anghel, I. G. & Anglart, H. Post-dryout heat transfer to high-pressure water flowing upward in vertical channels with various flow obstacles. *International journal of heat and mass transfer* **55,** 8020–8031 (2012).

20. Richenderfer, A. J. *Experimental study of heat flux partitioning in pressurized subcooled flow boiling* PhD thesis (Massachusetts Institute of Technology, 2018).

21. Statham, B. A. *Measurement and Prediction of the Onset of Intermittent Dryout During Blowdown Transients for Upward Annular Flow* PhD thesis (2014).

22. Hurley, P. *et al.* in *Design of a High-Pressure Water Loop for Optical Fiber Measurement of Post-CHF Heat Transfer* (Mar. 2022).

23. Ribeiro, L. *et al. Spontaneous Raman scattering in optical fiber: experimental measurement* in *AIP Conference Proceedings* **1055** (2008), 159–162.

24. Hurley, P. *Application of Optical Fiber Sensors for Quenching Temperature Measurement* MA thesis (Virginia Polytechnic Institute and State University, 2020).

25. Hurley, P. & Duarte, J. P. *Fiber Optic Sensing Application in Quenching Temperature Measurement* in *2019 ANS Winter Meeting* (Washington, D.C., Nov. 2019).

26. Bowman, R., Mueller, A. & Nagle, W. Mean temperature difference in design. *Trans. ASME* **62,** 283–294 (1940).

27. Thulukkanam, K. *Heat exchanger design handbook* (CRC press, 2000).

28. Menon, E. S. *Transmission pipeline calculations and simulations manual* (Gulf Professional Publishing, 2014).

29. Moody, L. F. Friction factors for pipe flow. *Trans. Asme* **66,** 671–684 (1944).

30. Groeneveld, D., Cheng, S. & Doan, T. 1986 AECL-UO critical heat flux lookup table. *Heat transfer engineering* **7,** 46–62 (1986).

31. Avramova, M. N. & Salko, R. K. CTF Theory Manual. https://www.osti.gov/biblio/1340446 (May 2016).

32. Duarte, J. P. & Corradini, M. L. Hydraulic and heated equivalent diameters used in heat transfer correlations. *Nuclear Technology* **201,** 99–102 (2018).

33. Barnett, P. *A CORRELATION OF BURNOUT DATA FOR UNIFORMLY HEATED ANNULI AND ITS USE FOR PREDICTING BURNOUT IN UNIFORMLY HEATED ROD BUNDLES.* tech. rep. (Atomic Energy Establishment, Winfrith (England), 1966).

Appendices

Appendix A

Components and Working Conditions of Investigated Facilities

Table A.1: Main components of the investigated loops

Facility	**Main components**
Post-CHF Heat Transfer (PCHT) test facility (Michigan)	Reservoir tank, Circulation Pump, Pre-heater, Vacuum pump, Condenser, Pressurizer, Sub-cooler, Bypass, Regulation Valve
Reactor coolant system thermal hydraulic loop facility (RCS loop facility)	Reservoir tank, Feed pump, De-ionizer, Circulation pump, Pre-heater, Steam/Water separator, Condenser, Pressurizer, Cooler
Royal Institute of Technology (KTH), Stockholm, Sweden.	Feed pump, Circulation pump, Pre-heater, Condenser, Flow Measurement system, Filter
MIT Flow Boiling Experimental Facility	Chiller, Filters, Accumulator, Flow meter, Pre-heater, Pump, Vacuum Pump
McMaster University Flow boiling thermal-hydraulic circuit	Condenser, Subcoolers, Pressurizer/Accumulator, Circulation Pump, Flow Control Valves, Flow meter, Preheater

Appendix B

Sample Input File for CTF

```
************************************************************
*7 MPa at 500kg/m^2-s at 100 kJ/kg subcooling_Transient   *
************************************************************
*ICOBRA
      3
*INITIAL   DUMPF
       1       0
**    EPSO    OITMAX    IITMAX   COURANT
  0.000100       5        40    0.800000
*TITLE
PHILUS
************************************************************
*GROUP 1 - Calculation Variables and Initial Conditions   *
************************************************************
**NGR
   1
**NGAS IRFC EDMD IMIX ISOL GINIT   NOTRN  MESH  MAPS  IPRP  MFLX  IBTM  PPV  BWRM
   1    2    1    0    0    0.0     0     0     0     0     1     0     0    0
*Card 1.2
```

```
**         GTOT          AFLUX           DHFRAC        MFLUX
             0.0           10          0.0000000E+00     500
*Card 1.3
** PREF     HIN           HGIN       VFRAC1      VFRAC2
   70    1167.5      288.4200000   1.0000000   0.9999000
*Card 1.4
**GTP(1)   VFRAC(3)  GTP(2) VFRAC(4)  GTP(3) VFRAC(5)  GTP(4) VFRAC(6)
     air     0.0001
************************************************************
*GROUP 2 - Channel Description                             *
************************************************************
**NGR
    2
*Card 2.1
**  NCH NDM2 NDM3 NDM4 NDM5 NDM6 NDM7 NDM8 NDM9 NM10 NM11 NM12 NM13 NM14
      4    0    0    0    0    0    0    0    0    0    0    0    0    0
*Card 2.2
**   I          AN          PW       ABOT ATOP NMGP       X      Y     XSIZ     YSIZ
     1  0.21983E-04    0.18630E-01    0    0    0
     2  0.21983E-04    0.18630E-01    0    0    0
     3  0.21983E-04    0.18630E-01    0    0    0
     4  0.21983E-04    0.18630E-01    0    0    0

************************************************************
*GROUP 3 - Transverse Channel Connection (Gap) Data        *
************************************************************
```

```
**NGR
    3
*Card 3.1
**  NK NDM2 NDM3 NDM4 NDM5 NDM6 NDM7 NDM8 NDM9 NM10 NM11 NM12 NM13 NM14
     4    0    0    0    0    0    0    0    0    0    0    0    0    0
*Card 3.2
**   K    IK    JK        GAP     LNGT     WKR  FWAL IGPB IGPA FACT IGAP JGAP IGAP JGAP
*Card 3.3
**GMULT   ETNR
     1     1     2  0.236E-02  0.7552E-02  0.50  0    0    0  1.0    0    0    0    0
      1    0.0
     2     1     3  0.236E-02  0.7552E-02  0.50  0    0    0  1.0    0    0    0    0
      1    0.0
     3     2     4  0.236E-02  0.7552E-02  0.50  0    0    0  1.0    0    0    0    0
      1    0.0
     4     3     4  0.236E-02  0.7552E-02  0.50  0    0    0  1.0    0    0    0    0
      1    0.0
*Card 3.4
**NLGP
     0
************************************************************
*GROUP 4 - Vertical Channel Connection Data               *
************************************************************
**NGR
    4
*Card 4.1
```

```
**NSEC NSIM IREB NDM4 NDM5 NDM6 NDM7 NDM8 NDM9 NM10 NM11 NM12 NM13 NM14
     1    1    0    0    0    0    0    0    0    0    0    0    0    0
*Card 4.2
**ISEC    NCHN  NONO         DXS     IVAR
     1       4  132      0.1E-01        0
*Card 4.4
**    I   KCHA  KCHA  KCHA  KCHA  KCHA  KCHA   KCHB  KCHB  KCHB  KCHB  KCHB  KCHB
      1      1     0     0     0     0     0      1     0     0     0     0     0
      2      2     0     0     0     0     0      2     0     0     0     0     0
      3      3     0     0     0     0     0      3     0     0     0     0     0
      4      4     0     0     0     0     0      4     0     0     0     0     0
*Card4.5
**  IWDE
      4
*Card 4.6
**  MSIM
     528
************************************************************
*GROUP 8                                                   *
************************************************************
**NGR
    8
*Card 8.1
** NRRD   NSRD    NC  NRTB  NRAD  NLTY  NSTA   NXF  NCAN  RADF     W3  IHTC  DNBCHK  NDM
      1     0     1     1     0     0     1     1     0     0     -1    1      3      0
*Card 8.2
```

```
**    N   IFTY   IAXP  NRND  DAXMIN   RMULT    HGAP    ISECR  HTAMB   TAMB   SYMROD
*Card 8.3
**NSCH PIE    NSCH PIE    NSCH PIE    NSCH PIE    NSCH PIE    NSCH PIE      NSCH PIE
      1    1      1     0     0.0     1.000     0.0      1    0.000   0.000  1
   1  0.250     2 0.250     3 0.250     4 0.250    0  0.0     0  0.0          0  0.0
*Card 8.6
**    I   NRT1   NST1   NRX1
      1      1      0    2
*Card 8.7
**IRTB1  IRTB2  IRTB3  IRTB4  IRTB5  IRTB6  IRTB7  IRTB8  IRTB9 IRTB10 IRTB11 IRTB12
    1
*Card 8.9
**    AXIALT      TRINIT
 0.00000E+00 0.20000E+03
 0.13200E+01 0.20000E+03
************************************************************
*GROUP 9 - Conductor Geometry Description                  *
************************************************************
**NGR
    9
*Card 9.1
** NFLT IRLF ICNF IMWR NDM5 NDM6 NDM7 NDM8 NDM9 NM10 NM11 NM12 NM13 NM14
      1    0    0    0    0    0    0    0    0    0    0    0    0    0
*Card 9.6
**  I   FTYP       DROD        DIN  NFUL IMTO IMTI NDM8 NDM9 ND10 ND11 ND12 ND13 ND14
    1   tube     0.0095        0.00772   1     1    1    0    0    0    0    0    0
```

```
*Card 9.7
** NODER  MATR       TREG     QREG
       2     1   0.00089    1.0
************************************************************
*GROUP 10 - Material Properties Tables                    * ********************
**NGR
10
*Card 10.1
** NMAT NDM2 NDM3 NDM4 NDM5 NDM6 NDM7 NDM8 NDM9 NM10 NM11 NM12 NM13 NM14
      1    0    0    0    0    0    0    0    0    0    0    0    0    0
*Card 10.2
**N  NNTDP    RCOLD          IMATAN
  1      6  8470.57    Inconel 600
*Card 10.3
**   TPROP      CPF1      THCF
       -73     0.377    13.400
        93     0.464    15.710
       204     0.485    17.440
       427     0.527    20.900
       649     0.586    24.790
       871     0.623    28.830
************************************************************
*GROUP 11 - Core Power Distribution Information         *
************************************************************
**NGR
   11
```

```
*Card 11.1
** NQA  NAXP   MNXN    NQ NGPFF   NQR  NDM7  NDM8  NDM9 NDM10 NDM11 NDM12 NDM13 NDM14
     1     1     6     2     0     1     0     0     0     0     0     0     0     0
*Card 11.2
**          YQA
    0.00000E+00
*Card 11.3
**   I   NAXN
     1      6
*Card 11.4
**         Y      AXIALZ
  0.000       0.00000000
  0.13000000  0.00000000
  0.13000001  1.00000000
  1.13000000  1.00000000
  1.13000001  0.00000000
  1.32000000  0.00000000
*Card 11.5
  0.0   1.0
 90.0   10.0
*Card 11.7
**          YQR
    0.00000E+00
*Card 11.8
**    FQR1      FQR2      FQR3      FQR4      FQR5      FQR6      FQR7      FQR8
 1.0000000       0         0         0    0     0 0 0
```

```
************************************************************
*GROUP 13 -  Boundary Condition Data                       *
************************************************************
**NGR
   13
*Card 13.1
** NBND   NKBD NFUN NGBD  NIBNDB BCVEL NDM7 NDM8 NDM9 NM10 NM11 NM12 NM13 NM14
      8      0    0    0    0     0    0    0    0    0    0    0    0    0
*Card 13.4
**Inlet b.c. ------------------------------------------------------------
** IBD1   IBD2 ISPC N1FN N2FN N3FN      BCVALUE1     BCVALUE2     BCVALUE3 INITGAS
    1      1   2   0   0   0     500.0      1167.5       0.0   1
    2      1   2   0   0   0     500.0      1167.5     0.0   1
    3      1   2   0   0   0      500.0      1167.5    0.0   1
    4      1   2   0   0   0      500.0      1167.5    0.0   1
**outlet b.c. -----------------------------------------------------------
    1     134   1   0   0   0   0.00000E+00    0.00000E+00    70.0   1
    2     134   1   0   0   0   0.00000E+00    0.00000E+00    70.0   1
    3     134   1   0   0   0   0.00000E+00    0.00000E+00    70.0   1
    4     134   1   0   0   0   0.00000E+00    0.00000E+00    70.0   1
************************************************************
*GROUP 14 - Output Options                                 *
************************************************************
**NGR
  -14
*Keys
```

```
  hdf5       0
  rod_vtk    0
  chan_edits 1
  rod_edits  1
  gap_edits  0
  fluid_vtk  0
  dnb_edits  1
  krylo_out  0
  convergence 1
  mass_out   0
  heat_out   0
  run_out    0
  end 14
************************************************************
*GROUP 15 - Time Domain Data                               *
************************************************************
**NGR
   15
*Card 15.1
**     DTMIN       DTMAX        TEND       EDINT      DMPINT       RTWFP
   0.1000E-06  0.100E+00   9.0000E+01  1.0000E+00  0.0000E+00  0.1000E+00
  -0.1000E-06  0.100E+00  2.0000E+01  1.0000E+00  0.0000E+00  0.1000E+00
************************************************************
*GROUP 18 - Convergence Criteria for Steady State Solve   *
************************************************************
**NGR
```

```
   18
*Card 18.1
**Global Energy Balance Criteria (%)
  0.10000
*Card 18.2
**Global Mass Balance Criteria (%)
  0.10000
*Card 18.3
**Fluid Energy Storage Criteria (%)
  0.50000
*Card 18.4
**Solid Energy Storage Criteria (%)
  0.50000
*Card 18.5
**Mass Storage Criteria (%)
  0.500000
```

Appendix C

Results of CTF simulations

Table C.1: CTF results for 7 MPa

Pressure (MPa)	7						
Mass Flux (kg/m²s)	**Inlet Subcooling (kJ/kg)**	**Power (kW)**	**Outlet Quality**	**Void Fraction**	**Local Heat Flux at CHF (kW/m²)**	**Corrected CHF in LUT (kW/m²)**	**Pressure Drop (kPa)**
500	100	59.00	0.81	0.97	1975.09	1917.09	45.69
500	200	63.00	0.79	0.97	2109.11	2048.41	44.15
500	300	66.00	0.78	0.97	2209.79	2128.25	42.16
500	400	69.00	0.76	0.97	2304.98	2253.71	40.28
1000	100	86.00	0.58	0.94	2877.08	2827.62	108.36
1000	200	90.00	0.55	0.93	3014.33	2963.16	96.51
1000	300	95.00	0.51	0.92	3181.40	3130.32	87.23
1000	400	100.00	0.49	0.92	3348.96	3261.59	78.87
1500	100	96.00	0.42	0.90	3214.92	3153.70	149.99
2000	100	100.00	0.31	0.86	3348.95	3285.47	176.67

Table C.2: CTF results for 9 MPa

Pressure (MPa)	9						
Mass Flux (kg/m²s)	**Inlet Subcooling (kJ/kg)**	**Power (kW)**	**Outlet Quality**	**Void Fraction**	**Local Heat Flux at CHF (kW/m²)**	**Corrected CHF in LUT (kW/m²)**	**Pressure Drop (kPa)**
500	100	51.00	0.75	0.96	1707.06	1665.08	31.85
500	200	54.00	0.73	0.95	1807.59	1755.98	30.24
500	300	57.00	0.71	0.95	1908.12	1836.18	28.79
500	400	60.00	0.69	0.95	2008.66	1960.45	27.47
1000	100	68.00	0.48	0.90	2276.74	2229.02	65.05
1000	200	74.00	0.46	0.89	2477.80	2405.05	58.97
1000	300	79.00	0.42	0.88	2645.35	2626.67	52.65
1000	400	85.00	0.40	0.87	2846.40	2790.62	48.16
1500	100	77.00	0.35	0.85	2578.33	2521.79	91.18
1500	200	85.00	0.32	0.83	2846.40	2787.89	78.71
1500	300	92.00	0.29	0.81	3080.96	3007.81	67.04
1500	400	99.00	0.25	0.79	3315.52	3228.56	57.32
2000	100	81.00	0.26	0.79	2712.36	2656.15	119.77
2000	200	90.00	0.22	0.76	3013.94	2960.63	89.98
2000	300	99.00	0.19	0.72	3315.52	3249.46	68.40
2500	100	84.00	0.20	0.74	2812.88	2761.65	125.75
2500	200	95.00	0.17	0.70	3181.48	3119.26	98.48
3000	100	87.00	0.16	0.69	2913.41	2867.91	141.38
3000	200	99.00	0.13	0.62	3315.52	3269.86	105.83
3500	100	89.00	0.14	0.64	2980.43	2943.89	154.44

Table C.3: CTF results for 11 MPa

Pressure (MPa)	11						
Mass Flux (kg/m²s)	**Inlet Subcooling (kJ/kg)**	**Power (kW)**	**Outlet Quality**	**Void Fraction**	**Local Heat Flux at CHF (kW/m²)**	**Corrected CHF in LUT (kW/m²)**	**Pressure Drop (kPa)**
500	100	41.00	0.65	0.93	1372.02	1331.93	21.87
500	200	45.00	0.63	0.92	1506.07	1480.52	21.23
500	300	48.00	0.62	0.92	1606.60	1539.96	20.25
500	400	52.00	0.59	0.91	1740.65	1692.73	19.84
1000	100	55.00	0.42	0.85	1841.19	1767.27	42.93
1000	200	61.00	0.38	0.84	2042.24	1973.83	38.74
1000	300	66.00	0.34	0.81	2243.30	2264.15	34.49
1000	400	72.00	0.33	0.80	2410.84	2357.84	31.65
1500	100	62.00	0.29	0.77	2075.75	2029.75	60.00
1500	200	69.00	0.25	0.74	2310.32	2261.27	50.39
1500	300	77.00	0.22	0.72	2578.39	2537.01	43.74
1500	400	86.00	0.19	0.69	2879.97	2842.66	39.26
2000	100	65.00	0.21	0.71	2176.28	2129.17	72.89
2000	200	75.00	0.18	0.66	2511.37	2472.97	59.99
2000	300	86.00	0.15	0.61	2879.97	2843.05	51.37
2000	400	97.00	0.12	0.57	3248.57	3178.86	44.82
2500	100	69.00	0.17	0.65	2310.32	2270.04	87.33
2500	200	82.00	0.13	0.59	2745.94	2693.49	71.12
2500	300	95.00	0.10	0.52	3181.56	3131.31	59.58
3000	100	73.00	0.14	0.59	2444.36	2400.47	102.31
3000	200	87.00	0.10	0.51	2913.50	2893.55	80.32
3500	100	77.00	0.11	0.54	2578.41	2549.11	117.93
3500	200	94.00	0.08	0.46	3148.06	3113.99	93.10

Table C.4: CTF results for 13 MPa

Pressure (MPa)	13						
Mass Flux (kg/m²s)	**Inlet Subcooling (kJ/kg)**	**Power (kW)**	**Outlet Quality**	**Void Fraction**	**Local Heat Flux at CHF (kW/m²)**	**Corrected CHF in LUT (kW/m²)**	**Pressure Drop (kPa)**
500	100	34.00	0.57	0.89	1137.51	1092.57	16.42
500	200	37.00	0.55	0.88	1238.05	1213.50	15.70
500	300	41.00	0.55	0.88	1372.09	1281.53	15.46
500	400	45.00	0.52	0.87	1506.13	1478.04	15.29
1000	100	45.00	0.35	0.78	1506.14	1480.37	30.88
1000	200	50.00	0.32	0.76	1673.70	1649.92	27.36
1000	300	56.00	0.28	0.73	1874.76	1845.01	25.12
1000	400	62.00	0.25	0.71	2075.81	2037.19	23.32
1500	100	50.00	0.24	0.69	1673.70	1631.65	42.91
1500	200	57.00	0.20	0.65	1908.27	1888.21	36.20
1500	300	66.00	0.17	0.61	2209.86	2171.22	32.53
1500	400	74.00	0.14	0.56	2477.93	2453.66	29.15
2000	100	55.00	0.18	0.62	1841.25	1809.04	55.83
2000	200	65.00	0.15	0.57	2176.35	2142.86	46.52
2000	300	76.00	0.12	0.51	2544.95	2482.72	40.65
2000	400	87.00	0.08	0.45	2913.55	2871.56	36.31
2500	100	60.00	0.15	0.56	2008.81	1972.48	69.84
2500	200	73.00	0.11	0.50	2444.43	2393.39	57.94
2500	300	86.00	0.08	0.43	2880.04	2826.52	49.81
2500	400	100.00	0.05	0.35	3349.16	3279.19	44.57
3000	100	65.00	0.13	0.52	2176.36	2157.99	85.00
3000	200	80.00	0.09	0.44	2679.00	2657.08	69.65
3000	300	96.00	0.06	0.36	3215.13	3191.40	60.14
3500	100	71.00	0.11	0.48	2377.42	2329.30	102.89
3500	200	88.00	0.07	0.40	2947.06	2920.46	83.57

Table C.5: CTF results for 15 MPa

Pressure (MPa)	15						
Mass Flux (kg/m²s)	**Inlet Subcooling (kJ/kg)**	**Power (kW)**	**Outlet Quality**	**Void Fraction**	**Local Heat Flux at CHF (kW/m²)**	**Corrected CHF in LUT (kW/m²)**	**Pressure Drop (kPa)**
500	100	28.00	0.52	0.85	936.49	916.01	13.09
500	200	32.00	0.50	0.84	1070.55	1054.82	12.96
500	300	35.00	0.47	0.82	1171.08	1147.97	12.63
500	400	38.00	0.45	0.81	1271.61	1236.34	12.38
1000	100	36.00	0.30	0.71	1204.61	1175.73	23.46
1000	200	42.00	0.27	0.68	1405.68	1348.81	21.48
1000	300	47.00	0.22	0.63	1573.23	1558.34	19.60
1000	400	53.00	0.19	0.59	1774.29	1743.83	18.53
1500	100	42.00	0.21	0.61	1405.68	1379.99	34.36
1500	200	50.00	0.17	0.56	1673.77	1651.69	29.99
1500	300	58.00	0.13	0.50	1941.85	1911.13	26.88
1500	400	66.00	0.10	0.44	2209.92	2187.13	24.48
2000	100	50.00	0.17	0.56	1673.77	1644.96	48.54
2000	200	59.00	0.13	0.50	1975.36	1937.82	40.38
2000	300	70.00	0.09	0.42	2343.95	2276.47	35.89
2000	400	81.00	0.05	0.34	2712.55	2656.44	32.52
2500	100	56.00	0.15	0.52	1874.83	1849.49	62.88
2500	200	68.00	0.10	0.44	2276.94	2256.16	52.30
2500	300	81.00	0.06	0.35	2712.55	2672.09	45.74
2500	400	94.00	0.03	0.26	3148.16	3123.29	40.98
3000	100	63.00	0.13	0.48	2109.40	2084.66	79.98
3000	200	77.00	0.09	0.40	2578.52	2545.44	65.80
3000	300	92.00	0.04	0.30	3081.14	3032.07	56.97
3500	100	69.00	0.12	0.46	2310.45	2280.58	97.77
3500	200	85.00	0.07	0.36	2846.58	2809.92	79.87

Table C.6: CTF results for 17 MPa

Pressure (MPa)	17						
Mass Flux (kg/m²s)	**Inlet Subcooling (kJ/kg)**	**Power (kW)**	**Outlet Quality**	**Void Fraction**	**Local Heat Flux at CHF (kW/m²)**	**Corrected CHF in LUT (kW/m²)**	**Pressure Drop (kPa)**
500	100	24.00	0.48	0.80	802.50	772.35	11.27
500	200	27.00	0.45	0.78	903.04	884.84	11.05
500	300	30.00	0.41	0.76	1003.57	993.11	10.92
500	400	33.00	0.38	0.73	1104.11	1079.36	10.83
1000	100	31.00	0.28	0.65	1037.11	1022.59	19.90
1000	200	36.00	0.22	0.58	1204.67	1191.30	17.98
1000	300	41.00	0.18	0.53	1372.23	1351.03	16.65
1000	400	47.00	0.15	0.48	1573.28	1543.52	16.00
1500	100	37.00	0.21	0.56	1238.19	1223.75	29.75
1500	200	45.00	0.16	0.49	1506.28	1482.72	26.21
1500	300	53.00	0.11	0.40	1774.35	1754.58	23.84
1500	400	61.00	0.07	0.32	2042.42	2005.55	22.19
2000	100	48.00	0.19	0.53	1606.80	1589.55	45.22
2000	200	56.00	0.13	0.44	1874.88	1846.20	37.42
2000	300	65.00	0.08	0.34	2176.46	2147.23	32.61
2000	400	86.00	-0.02	0.14	2880.09	2824.56	28.31
2500	100	55.00	0.17	0.49	1841.36	1820.09	60.18
2500	200	65.00	0.11	0.40	2176.45	2141.14	49.26
2500	300	77.00	0.06	0.29	2578.56	2511.25	43.02
2500	400	89.00	0.00	0.16	2980.64	2958.17	38.98
3000	100	61.00	0.15	0.45	2042.42	2019.79	76.11
3000	200	74.00	0.08	0.35	2478.03	2452.37	62.77
3000	300	87.00	0.03	0.23	2913.64	2850.49	53.83
3500	100	67.00	0.13	0.43	2243.47	2204.36	93.78
3500	200	81.00	0.07	0.31	2712.58	2677.41	76.13
3500	300	95.00	0.01	0.16	3181.70	3150.97	64.90